https://doi.org/10.5194/egusphere-2026-5224
Preprint. Discussion started: 28 September 2026

Charge-regulated aerosol survival from new particle formation to cloud condensation nuclei

Kunal Ghosh[1], Suneeti Mishra[2], and Gargi Sengupta[3]

[1]School of Earth, Environment and Sustainability, University of Leeds, Leeds, LS2 9JT, UK
[2]PSI Center for Energy and Environmental Sciences, 5232 Villigen PSI, Switzerland
[3]Environmental Research Group, School of Public Health, Imperial College London, White City Campus, Wood Lane, London W12 0BZ, UK

Correspondence: Kunal Ghosh (K.Ghosh@leeds.ac.uk)

Abstract. Cloud condensation nuclei (CCN) links atmospheric aerosol particles to cloud droplet formation, yet the electrical charge carried by these particles is not represented in aerosol-cloud models. Previous studies linking ionisation to CCN have focused on ion-induced particle production and found small effects. Here we test whether the natural bipolar charge distribution on all aerosol particles modifies particle survival and redistribution during growth to cloud-active sizes. Using the charge- and size-resolved ELSA-ICAM box model, we compare neutral and charged simulations in two regimes: a polluted urban regime dominated by sulfuric acid-dimethylamine nucleation and a clean boreal regime dominated by biogenic highly oxygenated organic molecule nucleation. In the polluted regime, bipolar charging reduces total particle number by 3.1% relative to the neutral case at 72 h while increasing CCN at 0.2% supersaturation by 2.5%. By 120 h, the number response reverses to $+4.1\%$ and the CCN enhancement increases to $+5.8\%$. In the clean regime, the charge-resolved case increases CCN by $+8.9\%$ at 120 h relative to the neutral case. Process attribution shows that charge-dependent coagulation is the largest shared contribution, increasing CCN by $+5.8\%$ in polluted air and $+5.3\%$ in clean air through size-selective survival and redistribution. Ion-induced nucleation is negligible in polluted air but contributes an additional $+3.6\%$ to CCN in clean air, despite producing a larger increase in particle number. The CCN response is therefore less sensitive to ion production than particle production. These results identify charge-regulated aerosol survival as a microphysical pathway linking atmospheric ionisation to CCN.

1 Introduction

Clouds exert a first-order control on the Earth's radiation budget, and the response of clouds to changing aerosol remains one of the largest sources of uncertainty in estimates of anthropogenic radiative forcing (Forster et al., 2021; Carslaw et al., 2013). The microphysical basis of this aerosol effect is well established. A greater concentration of aerosol particles able to activate into cloud droplets increases droplet number and raises cloud albedo for fixed liquid water content (Twomey, 1977). It can also modify cloud lifetime and precipitation efficiency (Albrecht, 1989). The strength of these effects is governed by the population of cloud condensation nuclei (CCN), and reducing uncertainty in CCN is therefore central to constraining the cloud radiative response (Grosvenor et al., 2018).

https://doi.org/10.5194/egusphere-2026-5224
Preprint. Discussion started: 28 September 2026

At a prescribed supersaturation, aerosol activation is determined primarily by particle dry size and chemical composition, the latter commonly represented by a hygroscopicity parameter and the mixing state of the aerosol population (Petters and Kreidenweis, 2007; Riemer et al., 2019). Activation parameterisations used in weather and climate models combine the size-resolved aerosol number and composition with atmospheric thermodynamic conditions and updraft velocity to calculate cloud-droplet number (Abdul-Razzak and Ghan, 2000). A substantial fraction of CCN does not originate from primary emissions but is produced through new particle formation (NPF) and subsequent growth (Merikanto et al., 2009; Gordon et al., 2017; Kerminen et al., 2018). Freshly nucleated particles must grow towards CCN-active sizes while avoiding coagulation scavenging by the pre-existing aerosol population. The probability of surviving this competition is classically expressed as a function of the ratio of the particle growth rate to the coagulation sink (Kerminen and Kulmala, 2002; Lehtinen et al., 2007). Because the coagulation sink increases steeply with decreasing particle size, survival is most strongly controlled by this growth–loss competition at the smallest sizes, where coagulation scavenging is generally the dominant loss process competing against growth; observational and theoretical studies accordingly focus on the sub-10 nm range, often resolved into intervals such as 1.5–3, 3–6, and 6–10 nm. This *nuclei survival* sets how many freshly formed particles persist beyond the cluster regime and determines the CCN formation efficiency of NPF (Pierce and Adams, 2007). The CCN yield, however, depends on survival across the full trajectory to cloud-active sizes: particles that clear the cluster regime can still be preferentially lost or redistributed by coagulation as they grow through the Aitken and accumulation modes. We refer to this broader, size-resolved competition as *aerosol survival*. The CCN yield of NPF is therefore controlled not only by how many particles form, but by which particles survive and grow across the entire size range (Deng et al., 2021). Any process that modifies this survival probability can consequently modify CCN.

Atmospheric aerosol particles are not generally electrically neutral. The lower atmosphere is continuously ionised by galactic cosmic rays, radioactive decay of radon and its progeny, and terrestrial gamma radiation. These processes produce small ions that sustain atmospheric conductivity and the global electric circuit (Bazilevskaya et al., 2008; Rycroft et al., 2008; Tinsley, 2008). Small ions attach to aerosol particles, producing a continuously regenerated distribution of positive, neutral, and negative particles (Hoppel and Frick, 1986; Harrison and Carslaw, 2003; Hirsikko et al., 2011). Charged aerosol has been observed in fair-weather conditions, at cloud edges (Nicoll and Harrison, 2016), in volcanic plumes (Gilbert et al., 1991; Harrison et al., 2010), in elevated mineral dust (Nicoll et al., 2011), and in the stratosphere (Renard et al., 2013; Brattich et al., 2019). Charge is therefore a persistent property of atmospheric aerosol, but it is absent from the aerosol state variables represented in most weather and climate models.

The microphysical effects of charge are also well established. Ions can lower the free-energy barrier to cluster formation and thereby enhance particle formation under favourable atmospheric conditions. Ion-mediated particle formation was explored theoretically by Yu and Turco (2001), while the importance of ion-induced nucleation under clean conditions was subsequently demonstrated experimentally by the CERN CLOUD studies (Kirkby et al., 2011, 2016). In addition to the charge present at the point of NPF, existing particles acquire charge through ion-aerosol attachment at rates that depend on particle size and the ambient small-ion population (Hoppel and Frick, 1986). Charge subsequently modifies coagulation. Coulomb attraction between oppositely charged particles enhances their collision rate, whereas repulsion between similarly charged particles

https://doi.org/10.5194/egusphere-2026-5224
Preprint. Discussion started: 28 September 2026

suppresses it. Image-charge and van der Waals interactions further modify the collision kernel (Ghosh et al., 2017, 2021). Electrostatic forces can also alter the scavenging of interstitial aerosol by cloud droplets (Tinsley et al., 2000; Laakso et al., 2002). These processes act directly on aerosol number and size, the quantities that determine particle survival and eventual activation as CCN.

The connection between atmospheric ionisation and CCN has nevertheless been examined largely through the particle-formation pathway. Motivated by the hypothesis that solar modulation of the cosmic-ray flux influences cloud cover (Svensmark and Friis-Christensen, 1997; Carslaw et al., 2002), global modelling and chamber-constrained studies have asked whether variability in ionisation changes CCN by changing the ion-induced nucleation rate. These studies generally found only a small CCN response to variations in air ion concentrations (or ionisation rates) because many of the additional particles are lost by coagulation before reaching CCN-active sizes, while competition for condensable vapour can limit the growth of those that survive (Pierce and Adams, 2009; Dunne et al., 2016). This conclusion addresses the production pathway, but it does not fully address a separate survival pathway. Even without variability in the ion source, the charge carried by existing aerosol particles modifies the coagulation processes that govern their survival.

Production and survival therefore represent distinct pathways. The production pathway asks whether ions create additional particles, whereas the survival pathway asks whether particle charge changes which particles persist and grow to CCN-active sizes. Previous ion–aerosol modelling followed the evolution of charged and neutral particles from molecular clusters to approximately 20 nm diameter (Yu and Turco, 2001). However, to our knowledge, no study has quantified this pathway across the complete NPF-to-CCN transition by following an evolving atmospheric aerosol population jointly in size and charge through particle formation, growth, coagulation, and post-NPF aging to supersaturation-dependent CCN. Furthermore, this pathway has not been tested using matched controls in contrasting polluted and clean environments. This distinction is important because charge can have a small effect through particle production while exerting a measurable influence on CCN through particle survival.

Here, we test the survival pathway directly using ELSA-ICAM, the Electrical State of Aerosol extension of the Integrated Chemistry Aerosol Microphysics (ICAM) model (Ghosh et al., 2026), which resolves the aerosol population jointly by particle size and integer charge state. The model couples a prognostic bipolar small-ion balance with ion attachment to aerosol (Hoppel and Frick, 1986), neutral and ion-induced nucleation, condensation, dry deposition, and charge-resolved coagulation. The coagulation kernel accounts for Coulomb, image-charge, and van der Waals interactions across all particle size and charge-state combinations. Coagulation is integrated using the volume- and charge-conserving numerical scheme described by Ghosh et al. (2017, 2021). We address four questions. First, does bipolar charge acquired under ordinary atmospheric ionisation measurably alter the evolution of an NPF population and its conversion to CCN? Second, which of ion-induced nucleation, charge-modified condensation, and charge-dependent coagulation contributes most strongly to the CCN response? Third, how does the dominant process redistribute particle number across the size distribution and thereby affect particle survival to CCN-active sizes? Fourth, does this response persist across contrasting polluted and clean aerosol environments?

We find that ordinary atmospheric particle charging alters the pathway from particle formation to CCN across both polluted and clean regimes, even though the corresponding particle-number responses differ strongly. Charge-dependent coagulation provides the dominant shared contribution to the CCN response in both environments, while ion-induced nucleation provides an additional production pathway in the clean regime whose large effect on particle number is strongly filtered before particles reach CCN-active sizes. On this basis, we propose the *charge-regulated aerosol survival* hypothesis, in which particle charge influences CCN primarily by modifying which particles survive and are redistributed to cloud-active sizes during growth and aging.

2 Methods

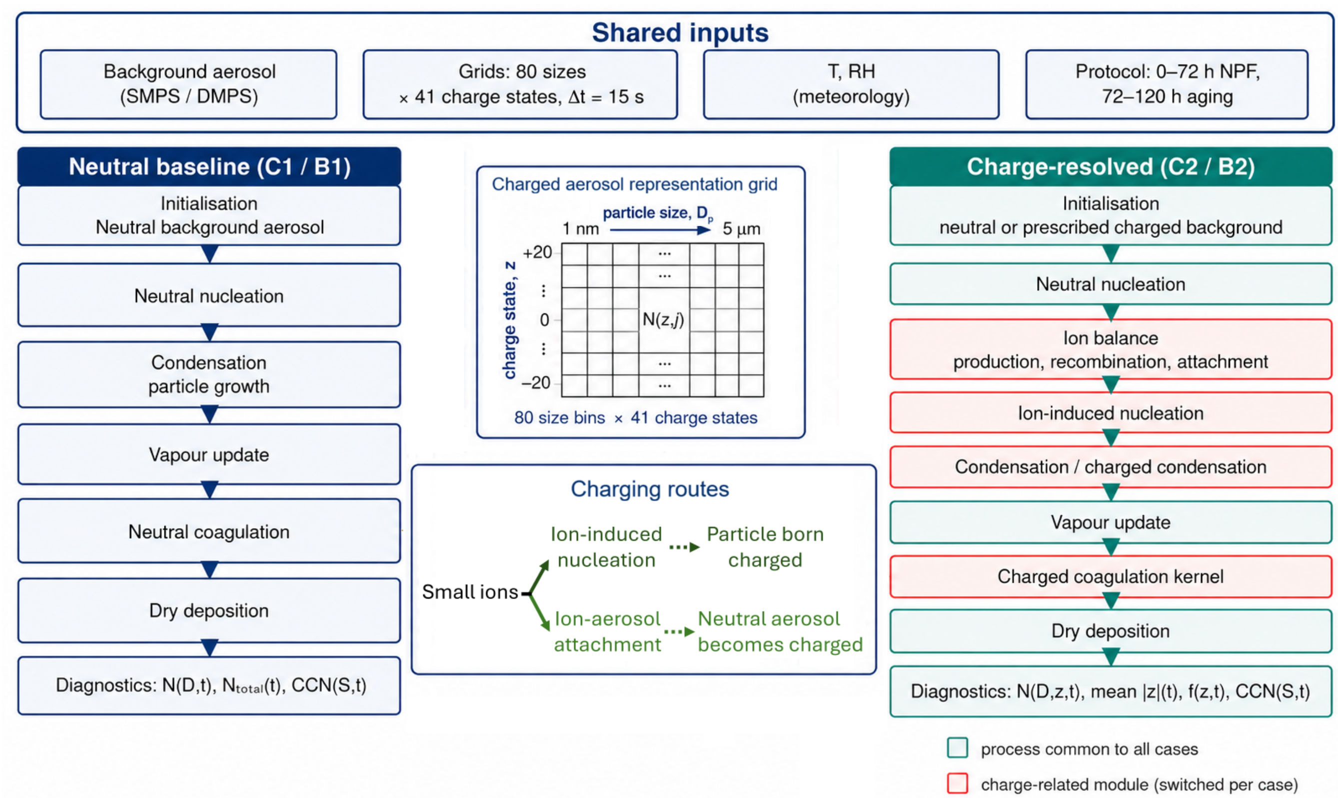

Figure 1. Architecture of ELSA-ICAM and the two-regime experiment design. The neutral references C1 and B1 (left) and the corresponding charge-resolved C2 and B2 experiment families (right) use the same inputs within each atmospheric regime. All simulations resolve 80 particle-size bins, while the charge-resolved experiments additionally resolve 41 integer charge states ($z = -20, \ldots, +20$), represented schematically by the charged aerosol representation grid in the centre. Aerosol particles acquire charge through two routes: ion-induced nucleation creates particles directly in a charged state, whereas ion–aerosol attachment transfers initially neutral or already charged particles between charge states. All simulations use a timestep of $\Delta t = 15\,\mathrm{s}$ and follow 72 h of active new particle formation (NPF) followed by 48 h of post-NPF aging. The polluted and clean regimes use different measured background aerosol distributions, meteorology, nucleating vapours, and condensation treatments, as described in Sect. 2.2. Charge-related modules that are switched among the attribution experiments are highlighted in red; the complete experiment hierarchy and process switches are given in Table 1.

https://doi.org/10.5194/egusphere-2026-5224
Preprint. Discussion started: 28 September 2026

The overall ELSA-ICAM architecture and experiment hierarchy are summarised in Fig. 1, and the process configuration of each experiment is listed in Table 1. We apply the same numerical framework to two contrasting atmospheric regimes. The polluted configuration is constrained by wintertime Delhi observations and uses sulfuric-acid– dimethylamine nucleation and sulfuric-acid condensation. The clean configuration is constrained by Hyytiälä SMEAR II observations and uses pure-biogenic highly oxygenated organic molecule (HOM) nucleation together with volatility-resolved organic condensation. Within each regime, the neutral and charge-resolved simulations use identical initial aerosol, meteorology, vapour forcing, size grid, deposition treatment, and integration protocol.

The neutral references are denoted C1 for the polluted regime and B1 for the clean regime. The C2 and B2 experiment families introduce a prognostic bipolar small-ion balance and resolve the evolving aerosol charge distribution. Incremental process switches isolate charge-dependent coagulation, regime-specific ion-induced nucleation, and charge-enhanced sulfuric-acid condensation. The complete charge-resolved configurations are C2c and B2c. The neutral-kernel controls C2-NK and B2-NK retain the ion balance, charge bookkeeping, and ion attachment but replace all charge-dependent aerosol collision coefficients with the neutral Brownian kernel. Ion-induced nucleation and charge-enhanced condensation are disabled in these numerical controls, allowing them to reproduce C1 and B1 to numerical precision.

Table 1. Overview of the model experiments and their charge-related process configuration, including ion production and attachment (IPA), charged-dependent coagulation (CDC), ion-induced nucleation (IIN), charge-enhanced condensation (CEC), initial aerosol charge state (z_0), and experimental purpose for each case used in this study. A filled circle denotes an active process for that case while – denotes an inactive process.

Case	Regime	IPA	CDC	IIN	CEC	Purpose
C1	Polluted	–	–	–	–	Neutral reference
C2-NK	Polluted	•	neutral	–	–	Numerical charge-bookkeeping control
C2	Polluted	•	•	–	–	Charge-dependent coagulation
C2b	Polluted	•	•	inorganic	–	Adds sulfuric-acid–water IIN
C2c	Polluted	•	•	inorganic	•	Complete polluted charge configuration
B1	Clean	–	–	–	–	Neutral reference
B2-NK	Clean	•	neutral	–	–	Numerical charge-bookkeeping control
B2a	Clean	•	•	–	–	Charge-dependent coagulation
B2b	Clean	•	•	biogenic	–	Adds bipolar HOM IIN
B2c	Clean	•	•	biogenic	•	Complete clean charge configuration

2.1 Charge-resolved ELSA-ICAM framework

We use ELSA-ICAM, the charge-resolved extension of the neutral box-model component of the 3D-ICAM framework (Ghosh et al., 2026). The model represents a well-mixed aerosol population jointly by particle dry size and integer elementary charge.

https://doi.org/10.5194/egusphere-2026-5224
Preprint. Discussion started: 28 September 2026

Its state variable $N_{z,j}$ is the number concentration in charge state z and size bin j. The charged simulations use 41 charge states, $z = -20, \ldots, +20$, while all simulations use 80 size bins. Number concentrations are expressed in cm^{-3} per size–charge bin.

The aerosol grid contains 80 logarithmically spaced volume bins spanning dry particle diameters from 1 nm to 5 μm (Fig.1). The representative particle volume in size bin j is $V_j = \pi D_j^3/6$. Nucleation, condensation, and coagulation products are transferred between adjacent sectional bins using volume-conserving interpolation. The charge-resolved general dynamic equation is written schematically as

$$\frac{\mathrm{d}N_{z,j}}{\mathrm{d}t} = S^{\mathrm{neu}}_{z,j} + S^{\mathrm{ion}}_{z,j} + \mathcal{G}_{z,j} + \mathcal{A}_{z,j} + \mathcal{K}_{z,j} - \Lambda_j N_{z,j}, \tag{1}$$

where S^{neu} and S^{ion} are the neutral and ion-induced particle-formation sources, $\mathcal{G}$ is condensational transport across the size grid, $\mathcal{A}$ is redistribution among charge states by ion attachment, $\mathcal{K}$ is coagulation, and Λ_j is the size-dependent dry-deposition loss rate. Summing Eq. (1) over charge states gives the corresponding size-resolved equation.

All simulations are run for 120 h with a time step of 15 s. Neutral and ion-induced nucleation are active during the first 72 h and are then switched off, followed by 48 h of post-NPF aging. The hourly temperature and relative-humidity measurements for a representative day in each regime are interpolated to the model time step and repeated as a 24 h cycle over the five simulation days. Within a time step, operators are applied in the following order: neutral nucleation; small-ion production, recombination, and attachment; ion-induced nucleation; condensation and vapour update; coagulation; and dry deposition (Fig. 1).

2.2 Initial aerosol and gas-phase inputs

For both regimes, measured mobility-size distributions reported as $\mathrm{d}N/\mathrm{d}\log_{10} D_p$ are converted to channel-integrated number concentrations according to

$$N_i = \left(\frac{\mathrm{d}N}{\mathrm{d}\log_{10} D_p}\right)_i \Delta \log_{10} D_{p,i}. \tag{2}$$

Each measured channel is assigned to the model size interval containing its representative diameter, and its integrated number is added to that model bin. Model bins outside the measured diameter range are initialised with zero background number. No additional background-number scaling is applied. Neutral cases place the complete initial distribution in $z = 0$. All charged cases also begin at $z = 0$, after which bipolar ion attachment generates the charge distribution prognostically.

2.2.1 Polluted configuration

The polluted initial aerosol and meteorological cycles are based on the wintertime Delhi SMPS observations reported by Mishra et al. (2023). A representative background spectrum is obtained by averaging selected low-number days on which no NPF event was identified. The mapped initial distribution has a total number concentration of approximately $1.97 \times 10^3\,\mathrm{cm}^{-3}$ and is used without concentration scaling.

The initial sulfuric-acid concentration is $[\mathrm{H_2SO_4}]_0 = 1.0 \times 10^6\,\mathrm{cm}^{-3}$. During active NPF, its prescribed production rate is

$$P_{\mathrm{H_2SO_4}}(t) = P_{\min} + (P_{\max} - P_{\min}) \exp\left[-\frac{(t_{\mathrm{day}} - 12\,\mathrm{h})^2}{2(2\,\mathrm{h})^2}\right], \tag{3}$$

https://doi.org/10.5194/egusphere-2026-5224
Preprint. Discussion started: 28 September 2026

where $P_{\min} = 1.0 \times 10^6$ and $P_{\max} = 5.0 \times 10^6\,\mathrm{cm^{-3}\,s^{-1}}$. The same 24 h source cycle is repeated on each active-NPF day. Dimethylamine is held fixed at $[\mathrm{DMA}] = 5.0 \times 10^6\,\mathrm{cm^{-3}}$ and is not depleted by nucleation. Sulfuric acid evolves prognostically as

$$[\mathrm{H_2SO_4}]^{n+1} = \max\{0, [\mathrm{H_2SO_4}]^n + \Delta t\,(P_{\mathrm{H_2SO_4}} - L_{\mathrm{nuc}} - L_{\mathrm{cond}})\}\,, \tag{4}$$

where L_{nuc} includes the vapour consumed by neutral and ion-induced particle formation and L_{cond} is the condensation loss to the evolving aerosol. Nucleation is disabled after 72 h. The background source $P_{\min}$ is retained during aging, and the post-NPF vapour treatment is applied identically to all polluted matched cases.

2.2.2 Clean configuration

The clean initial aerosol is obtained from Hyytiälä SMEAR II DMPS observations accessed through the Smart-SMEAR database (Junninen et al., 2009). We use 9 March 2020, a complete non-NPF day preceded by seven complete non-NPF days, to represent an aged accumulation-mode background with a low condensation sink. The daily-median size distribution has an integrated number concentration of approximately $1.02 \times 10^3\,\mathrm{cm^{-3}}$, a number mode near 178 nm, and a median sulfuric-acid condensation sink of approximately $2.9 \times 10^{-3}\,\mathrm{s^{-1}}$. The 24 h temperature and relative-humidity cycles are taken from the same day.

A prescribed sulfuric-acid concentration cycle of approximately 1.0×10^5 to $1.0 \times 10^6\,\mathrm{cm^{-3}}$ is used during active NPF, consistent with concentrations observed under boreal conditions (Riipinen et al., 2007). After 72 h, sulfuric acid is held at the minimum of this cycle. Organic nucleation and growth are driven by a prognostic total HOM reservoir. A preliminary neutral B1 simulation is used to derive a 24 h external HOM production profile from a reference HOM concentration cycle of 5.0×10^7 to $1.0 \times 10^8\,\mathrm{cm^{-3}}$ obtained from Zha et al. (2018). The resulting production profile, $P_{\mathrm{HOM}}(t)$, is fixed, repeated every 24 h, and applied without retuning to B1 and all B2 experiments. HOM concentrations then evolve prognostically in response to condensation and particle formation. Changes in the aerosol population can therefore alter the condensation sink and the HOM available for subsequent nucleation and growth. The imposed HOM forcing is literature constrained but is not intended to reproduce a measured HOM time series.

2.3 Neutral nucleation and condensational growth

2.3.1 Polluted H_2SO_4–DMA system

Neutral particle formation in the polluted regime follows the H_2SO_4–DMA cluster-kinetic treatment of Brean et al. (2023), as used in the neutral 3D-ICAM box configuration (Ghosh et al., 2026). The neutral formation rate depends on H_2SO_4, DMA, temperature, relative humidity, and the sink imposed by the existing aerosol. Newly formed neutral particles have a target diameter of 1.5 nm and are inserted into $z = 0$ using volume-conserving interpolation. H_2SO_4 condensation follows the transition-regime treatment of Laakso et al. (2002). Condensation is solved semi-implicitly as transport between adjacent size

https://doi.org/10.5194/egusphere-2026-5224
Preprint. Discussion started: 28 September 2026

pivots, with particle charge preserved during growth. The corresponding aerosol uptake is included in the prognostic H_2SO_4 budget in Eq. (4).

2.3.2 Clean HOM system

Pure-biogenic neutral nucleation follows the CLOUD parameterisation of Kirkby et al. (2016). Defining $H = [\mathrm{HOM}]/(10^7\,\mathrm{cm}^{-3})$, the neutral formation rate at 1.7 nm mobility diameter is

$$J_{\mathrm{n,HOM}} = a_1 H^{a_2 + a_5/H}, \tag{5}$$

with $a_1 = 0.04001$, $a_2 = 1.848$, and $a_5 = 0.1863$. The corresponding physical diameter used for sectional insertion is 1.4 nm. Newly formed neutral particles are inserted into $z = 0$ using volume-conserving interpolation.

The clean HOM concentration is obtained from

$$\frac{\mathrm{d[HOM]}}{\mathrm{d}t} = P_{\mathrm{HOM}}(t) - L_{\mathrm{cond,HOM}} - \nu_{\mathrm{HOM}}\left(J_{\mathrm{n,HOM}} + J_{\mathrm{i,HOM}}\right), \tag{6}$$

where ν_{HOM} is the number of HOM molecules represented by a new 1.4 nm particle. This concentration is integrated prognostically and constrained to remain non-negative.

Organic condensational growth is represented using a reduced nine-bin Kelvin-volatility-basis-set treatment of Tröstl et al. (2016). The nine saturation-concentration bins are $\log_{10}(C^*/\mu\mathrm{g\,m^{-3}}) = -8, -7, \ldots, 0$. The total prognostic HOM reservoir is partitioned among these bins using the adopted OBS-LVOC88 profile: 7.1 % extremely low-volatility organic compounds, 88.0 % low- volatility organic compounds, and 4.9 % semi-volatile organic compounds. The bin fractions are 3.29, 0.78, 1.04, 1.99, 10.0, 18.0, 35.0, 25.0, and 4.90 %, respectively. Uptake includes transition-regime transport and the Kelvin effect, using a representative molar mass of $300\,\mathrm{g\,mol^{-1}}$, density of $1400\,\mathrm{kg\,m^{-3}}$, surface tension of $0.023\,\mathrm{N\,m^{-1}}$, and accommodation coefficient of unity. The model retains one prognostic total-HOM gas reservoir rather than nine independently prognostic chemical tracers.

2.4 Small-ion balance and ion–aerosol attachment

Positive and negative small ions are produced symmetrically at an ion-pair production rate q. The simulations use $q = 5.0\,\mathrm{cm^{-3}\,s^{-1}}$; sensitivity simulations use $q = 2.0$ and $10.0\,\mathrm{cm^{-3}\,s^{-1}}$. Their concentrations evolve according to

$$\frac{\mathrm{d}n^+}{\mathrm{d}t} = q - \alpha n^+ n^- - n^+ \sum_{z,j} K^+_{z,j} N_{z,j}, \tag{7a}$$

$$\frac{\mathrm{d}n^-}{\mathrm{d}t} = q - \alpha n^+ n^- - n^- \sum_{z,j} K^-_{z,j} N_{z,j}. \tag{7b}$$

where $\alpha = 1.6 \times 10^{-6}\,\mathrm{cm^3\,s^{-1}}$ is the bipolar ion–ion recombination coefficient and $K^{\pm}_{z,j}$ are the size- and charge-dependent ion-attachment coefficients (Hoppel and Frick, 1986). $K^{\pm}_{z,j}$ depends on the small-ion diffusivity as well as the electrostatic interaction between the ion and the charged aerosol particle. We assume the positive- and negative-ion diffusivities are constant

https://doi.org/10.5194/egusphere-2026-5224
Preprint. Discussion started: 28 September 2026

and equal, $D_+ = D_- = 0.035\,\mathrm{cm^2\,s^{-1}}$. Initial small-ion concentrations are obtained from the steady-state solution of Eq. (7) for the initially neutral aerosol distribution of the corresponding regime.

Attachment of a positive ion transfers a particle from z to $z+1$; attachment of a negative ion transfers it from z to $z-1$. The same event rates update both the aerosol charge matrix and the small-ion concentrations. The attachment and ion–ion recombination operator therefore conserves aerosol number and the net charge of the combined aerosol–small-ion system to numerical precision. The operator is integrated with adaptive explicit subcycling, a target ion-loss Courant number of 0.05, and a maximum substep of 5 s. Attempted transitions beyond the finite charge grid are blocked and diagnosed.

2.5 Ion-induced nucleation

The two regimes use chemically distinct IIN parameterisations. In the polluted C2b and C2c experiments, negative-ion-mediated binary sulfuric-acid– water nucleation follows Dunne et al. (2016). The uncapped rate at 1.7 nm is

$$J^*_{\mathrm{i,H_2SO_4}} = k_{\mathrm{bi}}(T)\,n^- \left(\frac{[\mathrm{H_2SO_4}]}{10^6\,\mathrm{cm^{-3}}}\right)^{3.37}, \tag{8}$$

where

$$\ln k_{\mathrm{bi}}(T) = -11.5 - \exp\left[25.5\left(\frac{T}{1000\,\mathrm{K}} - 0.181\right)\right]. \tag{9}$$

The applied rate is limited by ion production and the available negative small-ion population:

$$J_{\mathrm{i,H_2SO_4}} = \min\left[J^*_{\mathrm{i,H_2SO_4}}, q, 0.95\frac{n^-}{\Delta t}\right]. \tag{10}$$

Each event consumes one negative ion and produces a particle in $z = -1$. Sulfuric acid represented by the new particle is removed from the vapour budget. This channel does not consume DMA.

In the clean B2b and B2c experiments, HOM IIN follows Kirkby et al. (2016). Positive- and negative-ion branches are evaluated separately using the prognostic ion concentrations:

$$J^+_{\mathrm{i,HOM}} = a_3 n^+ H^{a_4 + a_5/H}, \tag{11}$$

$$J^-_{\mathrm{i,HOM}} = a_3 n^- H^{a_4 + a_5/H}, \tag{12}$$

$$J_{\mathrm{i,HOM}} = J^+_{\mathrm{i,HOM}} + J^-_{\mathrm{i,HOM}}, \tag{13}$$

where $a_3 = 0.001366$, $a_4 = 1.566$, and $a_5 = 0.1863$. Each positive or negative branch consumes one ion of the corresponding polarity and creates a particle with charge $z = +1$ or $z = -1$, respectively. New particles are inserted at a physical diameter of 1.4 nm using volume-conserving interpolation. The HOM represented by these particles is removed through Eq. (6).

2.6 Charge-resolved coagulation

The charge-resolved coagulation coefficient for particles in size bins j and k and charge states z and z' is

$$K^{zz'}_{jk} = \beta^{\mathrm{B}}_{jk} A^{zz'}_{jk}, \tag{14}$$

https://doi.org/10.5194/egusphere-2026-5224
Preprint. Discussion started: 28 September 2026

where β^{B}_{jk} is the neutral Brownian kernel and $A^{zz'}_{jk}$ is a precomputed interaction correction containing Coulomb, image-charge, and van der Waals interactions (Ghosh et al., 2017, 2021). The correction is normalised so that neutral–neutral collisions reproduce the Brownian kernel exactly. Collisions between particles carrying opposite charge are generally enhanced, whereas collisions between particles carrying similar charge are generally suppressed. The magnitude depends on both particle sizes and both charge states.

A collision produces a particle with charge $z_{\mathrm{p}} = z + z'$ and volume $V_{\mathrm{p}} = V_j + V_k$. Product volume is mapped between adjacent size pivots using volume-conserving interpolation. Coagulation is integrated with a sequential semi-implicit sectional solver. Same-size charge coupling is treated implicitly, while production into larger size bins is passed forward through the grid. The method conserves aerosol volume and charge, subject to the finite size and charge grids. Charge-boundary population, attempted charge overflow, and size overflow are recorded as numerical diagnostics. The neutral-kernel controls set $A^{zz'}_{jk} = 1$ for every charge pair.

2.7 Charge-enhanced condensation sensitivity

The complete C2c and B2c experiments apply a bounded sulfuric-acid condensation enhancement to charged particles between 1.8 and 3.2 nm, following the charge–dipole growth enhancement reported by Stolzenburg et al. (2020):

$$C_{z,j} = \begin{cases} 1.45 C^0_j, & z \neq 0 \text{ and } 1.8 \leq D_j \leq 3.2\,\mathrm{nm}, \\ C^0_j, & \text{otherwise}, \end{cases} \tag{15}$$

where C^0_j is the neutral sulfuric-acid condensation coefficient. The same coefficient is used in particle growth and in the corresponding sulfuric-acid condensation sink. The enhancement is applied symmetrically to both charge polarities. In the clean regime it modifies only the sulfuric-acid component; the nine-bin HOM uptake is not multiplied by this factor. This treatment is a bounded sensitivity, not a universal charge-dependent growth parameterisation.

2.8 Dry deposition

Dry removal is represented by a size-dependent first-order column loss (Zhang et al., 2001; Petroff and Zhang, 2010):

$$\Lambda_j = \frac{v_{\mathrm{dep},j}}{H} = \frac{v_{\mathrm{g},j} + v_{\mathrm{diff},j}}{H}, \tag{16}$$

where $H = 1000\,\mathrm{m}$ is the well-mixed column depth, $v_{\mathrm{g},j}$ is the gravitational settling velocity, and $v_{\mathrm{diff},j}$ is a simplified diffusion-dependent deposition velocity:

$$v_{\mathrm{diff},j} = \frac{u_*}{\mathrm{Sc}_j^{2/3} + 10}, \qquad \mathrm{Sc}_j = \frac{\nu}{D_{\mathrm{B},j}}. \tag{17}$$

Here $u_* = 0.30\,\mathrm{m\,s^{-1}}$, ν is the kinematic viscosity of air, and $D_{\mathrm{B},j}$ is the Brownian diffusivity. Diffusivity and settling velocity include the Cunningham slip correction. The same Λ_j is applied to every charge state, so direct charge-dependent deposition is not included.

https://doi.org/10.5194/egusphere-2026-5224
Preprint. Discussion started: 28 September 2026

2.9 CCN diagnosis

CCN concentrations are diagnosed from the dry size distribution using κ-Köhler theory (Petters and Kreidenweis, 2007). We use $\kappa = 0.30$ for the polluted aerosol and $\kappa = 0.18$ for the clean biogenic aerosol. The critical supersaturation is

$$s_{\mathrm{c},j} = \left(\frac{4A_{\mathrm{K}}^3}{27\kappa D_j^3}\right)^{1/2}, \qquad A_{\mathrm{K}} = \frac{4\sigma_{\mathrm{w}} M_{\mathrm{w}}}{RT\rho_{\mathrm{w}}}, \tag{18}$$

and

$$N_{\mathrm{CCN}}(s) = \sum_z \sum_{j:s_{\mathrm{c},j}\le s} N_{z,j}. \tag{19}$$

Diagnostics are calculated at supersaturations of 0.05, 0.075, 0.10, 0.15, 0.20, 0.30, 0.50, and 1.00 %. At 0.2 %, the corresponding dry activation diameters (D_{crit}) are approximately 95 nm for the polluted regime and 133 nm for the clean regime. Charge does not directly modify the activation calculation. Electro-Köhler corrections are excluded because the experiment is designed to isolate charge effects on particle formation, growth, and survival before activation.

2.10 Process attribution and numerical diagnostics

Process-resolved particle-number budgets are evaluated by recording the change in the aerosol state immediately before and after each operator. For process p, the contribution over a model step is

$$\Delta N^{(p)} = N_{\mathrm{after},p} - N_{\mathrm{before},p}. \tag{20}$$

The contributions are accumulated separately over active NPF (0–72 h) and aging (72–120 h). Attachment should conserve total particle number, while condensation should conserve number apart from sectional remapping residuals. During aging, physical changes in total number are therefore produced by coagulation and deposition.

Size-banded budgets are constructed from cumulative number changes above threshold diameters of 10, 25, 50, 100, 133, and 150 nm. For a band $D_a \le D_p < D_b$, the contribution is

$$\Delta N^{(p)}_{D_a - D_b} = \Delta N^{(p)}_{>D_a} - \Delta N^{(p)}_{>D_b}. \tag{21}$$

The < 10 nm contribution is the total contribution minus the contribution above 10 nm, and the final open band is $D_p > 150$ nm. The 133 nm threshold is retained because it approximates the clean-regime activation diameter at 0.2 % supersaturation.

Budget closure is evaluated after every time step by comparing the summed operator contributions with the diagnosed change in particle number. The uninstrumented and instrumented trajectories are also compared. Numerical diagnostics include the charge-grid boundary population, the fraction of attachment attempts at the charge boundary, coagulation charge overflow, the maximum coagulation-loss Courant number, and conservation of aerosol number, volume, and charge. The accepted calculations keep charge-boundary and overflow fractions far below 10^{-4} and show no numerical instability.

https://doi.org/10.5194/egusphere-2026-5224
Preprint. Discussion started: 28 September 2026

2.11 Model configuration and limitations

The principal numerical and physical settings are summarised in Table 2. The model is intentionally designed to isolate aerosol microphysical pathways. It does not represent dilution, entrainment, advection, cloud processing, externally imposed electric fields, space-charge transport, charge-dependent dry deposition, or direct electrostatic modification of droplet activation.

Table 2: Summary of the final two-regime ELSA-ICAM configuration and its principal assumptions.

Component	Implemented configuration	Notes and limitations
Geometry	Zero-dimensional, well-mixed box.	No spatial gradients, advection, entrainment, dilution, or cloud processing.
Size grid	80 logarithmically spaced volume bins from 1 nm to 5 μm.	Spherical particles and one representative volume per bin.
Charge grid	41 integer states, $z = -20, \ldots, +20$.	Boundary transitions and product-charge overflow are diagnosed.
Integration	120 h with $\Delta t = 15$ s for the simulations.	Active NPF from 0 to 72 h, followed by 48 h of aging. Budget terms are interpreted within regime.
Ion production	$q = 5.0\,\mathrm{cm^{-3}\,s^{-1}}$ in the runs; $q = 2.0$ and $10.0\,\mathrm{cm^{-3}\,s^{-1}}$ in sensitivity runs.	Equal positive- and negative-ion source rates; no spatial ion transport.
Initial aerosol	Delhi SMPS for the polluted regime; Hyytiälä DMPS for the clean regime; no number scaling.	Inputs are identical within each neutral–charged pair but differ between regimes.
Meteorology	Regime-specific measured 24 h temperature and RH cycles repeated over five model days.	No meteorological response to aerosol evolution.
Polluted vapour system	Prognostic H_2SO_4 with a repeated external source; fixed DMA.	Gas-phase chemistry is not solved explicitly.
Clean vapour system	Prognostic total HOM with fixed repeated $P_{\mathrm{HOM}}(t)$; prescribed low H_2SO_4.	The day-1 HOM reference is a high-HOM sensitivity, not a direct measured time series.
Neutral nucleation	H_2SO_4–DMA in polluted air; Kirkby HOM parameterisation in clean air.	Nucleation is disabled after 72 h.
Ion-induced nucleation	Negative-ion binary inorganic pathway in polluted air; bipolar HOM pathway in clean air.	Both consume the corresponding small ions and vapour represented by the new particles.

Continued on next page

https://doi.org/10.5194/egusphere-2026-5224
Preprint. Discussion started: 28 September 2026

Table 2 continued

Component	Implemented configuration	Notes and limitations
Condensation	Transition-regime H_2SO_4 uptake in both regimes; reduced nine-bin Kelvin-VBS HOM uptake in the clean regime.	The VBS uses one prognostic total-HOM reservoir rather than nine independent tracers.
Charged condensation	Factor 1.45 for charged particles from 1.8 to 3.2 nm, applied to H_2SO_4 uptake in C2c and B2c.	Bounded sensitivity; HOM uptake is not multiplied by this factor.
Coagulation	Brownian kernel multiplied by the charge-interaction correction of Ghosh et al. (2017, 2021).	Includes Coulomb, image-charge, and van der Waals interactions; product volume and charge are conserved.
Deposition	Size-dependent Brownian-diffusion loss and gravitational settling with $H = 1000\,\mathrm{m}$ and $u_* = 0.30\,\mathrm{m\,s^{-1}}$.	The same loss rate is applied to all charge states.
CCN	$\kappa = 0.30$ polluted; $\kappa = 0.18$ clean; supersaturation from 0.05 to 1.00 %.	Neutral κ-Köhler diagnosis; all charge states are summed.
Excluded processes	Spatial transport, imposed electric fields, cloud microphysics, charge-dependent deposition, and direct electro-Köhler activation.	The results quantify pre-activation aerosol evolution and CCN potential within a controlled box-model framework.

https://doi.org/10.5194/egusphere-2026-5224
Preprint. Discussion started: 28 September 2026

3 Results

3.1 Effect of charge on CCN

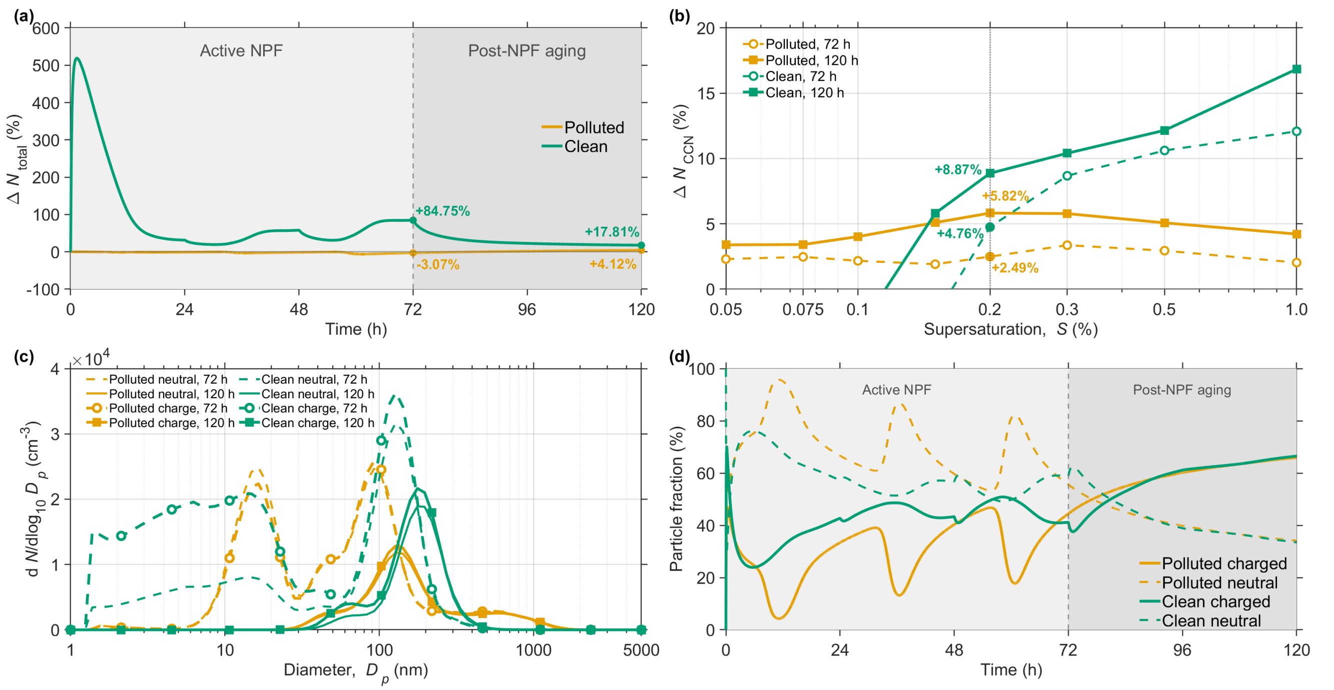

Figure 2. Effect of charge on (a) total particle number, shown as the relative difference $\Delta N_{\mathrm{total}}$ between the charged and neutral cases (C2c–C1 for polluted; B2c–B1 for clean) over 120 h; (b) CCN number, ΔN_{CCN}, for the same comparisons across supersaturation at 72 and 120 h, with the dotted line marking $0.2\,\%$ supersaturation; (c) dry particle size distributions of the neutral and full charged cases at 72 and 120 h; and (d) charged ($|z| > 0$) and neutral ($z = 0$) particle fractions in C2c and B2c. In (a) and (d), light- and dark-grey shading indicate active NPF and post-NPF aging, respectively, and the dashed line marks the end of nucleation at 72 h.

Figure 2 shows the effect of charge on total particle number (panel a), CCN (panel b), the particle size distribution (panel c), and the evolving aerosol charge state (panel d), for both polluted (orange) and clean (green) regimes. The charge treatment enhances CCN in both environments despite producing markedly different total-number responses. In the polluted regime, C2c contains $3.07\,\%$ fewer particles than C1 at the end of active NPF, whereas $N_{\mathrm{CCN},0.2}$ is $2.49\,\%$ higher. In the clean regime, B2c contains $84.75\,\%$ more particles than B1 at 72 h, but the corresponding enhancement in $N_{\mathrm{CCN},0.2}$ is only $4.76\,\%$. The much larger clean-regime response in total number reflects the additional ion-induced nucleation pathway in B2c. However, the disparity between the total-number and CCN responses shows that most of these additional particles have not reached cloud-active sizes by 72 h.

The responses evolve substantially during the subsequent 48 h aging period. In the polluted regime, the particle-number deficit reverses, and C2c contains $4.12\,\%$ more particles than C1 at 120 h. At the same time, the enhancement in $N_{\mathrm{CCN},0.2}$

https://doi.org/10.5194/egusphere-2026-5224
Preprint. Discussion started: 28 September 2026

increases from $2.49\,\%$ to $5.82\,\%$. In the clean regime, by contrast, the total-number enhancement decreases from $84.75\,\%$ at 72 h to $17.81\,\%$ at 120 h, while the enhancement in $N_{\mathrm{CCN},0.2}$ increases from $4.76\,\%$ to $8.87\,\%$ (Fig. 2a,b). Thus, aging removes much of the clean-regime excess in particle number while increasing the relative number of particles that reach CCN-active sizes.

The CCN response varies substantially with supersaturation (Fig. 2b). In the polluted regime, ΔN_{CCN} remains positive across the diagnosed supersaturation range at both 72 and 120 h, with the largest response near $0.2-0.3\,\%$. In the clean regime, the response is negative at lower supersaturations during active NPF and becomes positive as supersaturation approaches $0.2\,\%$. By 120 h, the transition to a positive response occurs at a lower supersaturation, and ΔN_{CCN} increases steadily with supersaturation. Because lower supersaturations activate only larger particles whereas higher supersaturations also activate smaller particles, this dependence shows that charge redistributes particle number selectively across CCN-relevant sizes rather than uniformly changing the CCN population.

The corresponding changes in the dry particle size distributions are shown in Fig. 2c. In the polluted regime, the charged case is depleted at smaller sizes but enhanced across the growing and accumulation modes, including near and above the critical activation diameter at $0.2\,\%$ supersaturation, $D_{\mathrm{crit}} \approx 95$ nm. In the clean regime, B2c contains a large excess of nucleation- and Aitken-mode particles at 72 h because of ion-induced production. Much of this excess is removed during aging, while the remaining population shifts towards larger sizes and becomes enhanced near and above $D_{\mathrm{crit}} \approx 133$ nm for the clean regime. Charging therefore changes both the survival of small particles and their redistribution towards cloud-active sizes, explaining why the CCN response can increase even when the total particle-number response decreases.

The charged and neutral particle fractions also evolve substantially over the simulation (Fig. 2d). Each particle-formation episode perturbs the balance between neutral and charged particles, after which ion–aerosol attachment progressively restores the charged fraction. Although the polluted and clean cases follow different trajectories during active NPF, both contain approximately $40\,\%$ charged particles at 72 h. Once nucleation is switched off, the charged fraction increases steadily in both regimes and reaches approximately $66\,\%$ by 120 h. Charge-mediated processes therefore remain active throughout post-NPF aging, when the CCN enhancement strengthens in both environments.

https://doi.org/10.5194/egusphere-2026-5224
Preprint. Discussion started: 28 September 2026

3.2 Charge process contribution

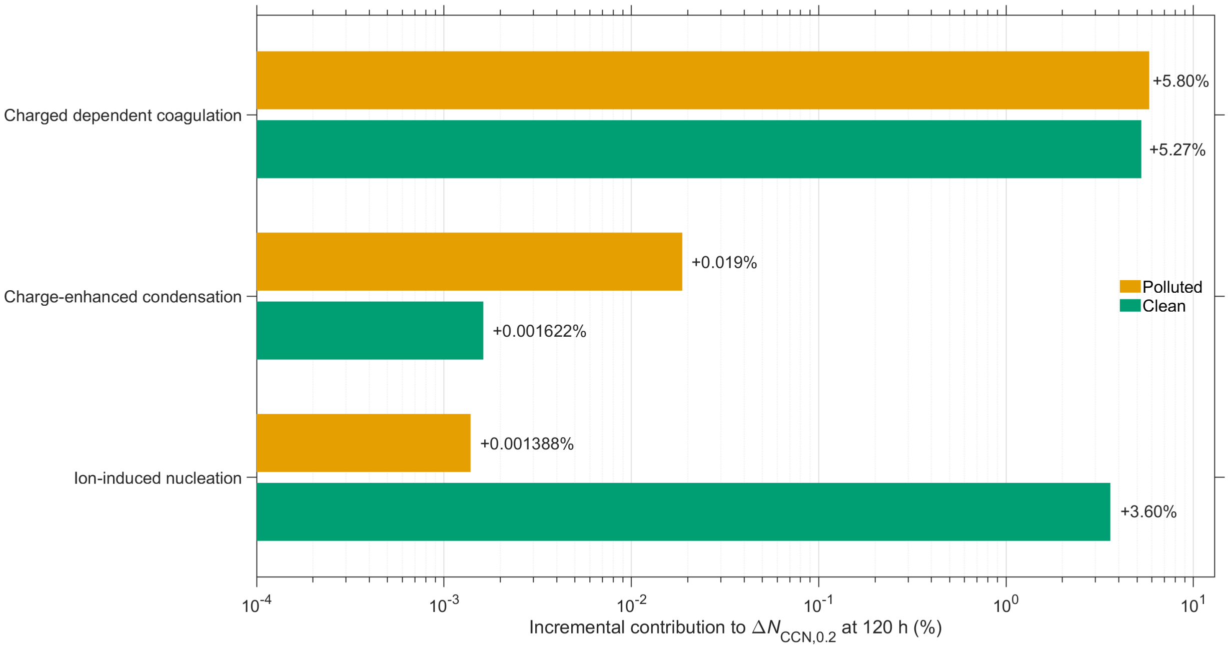

Figure 3. Sequential contributions of charge-dependent coagulation, ion-induced nucleation, and charge-enhanced condensation to $\Delta N_{\mathrm{CCN},0.2}$ at 120 h in the polluted and clean regimes. The contributions are defined by the prescribed experiment hierarchy and sum to the complete charge-related CCN response in each regime.

The experiment hierarchy in Table 1 separates the sequential contribution of each charge-related process through case comparisons. In the polluted regime, charge-dependent coagulation is quantified by $\mathrm{C2}-\mathrm{C1}$, ion-induced nucleation by $\mathrm{C2b}-\mathrm{C2}$, and charge-enhanced condensation by $\mathrm{C2c}-\mathrm{C2b}$. The corresponding clean comparisons are $\mathrm{B2a}-\mathrm{B1}$, $\mathrm{B2b}-\mathrm{B2a}$, and $\mathrm{B2c}-\mathrm{B2b}$, respectively. The resulting changes in $N_{\mathrm{CCN},0.2}$ at 120 h are shown in Fig. 3. Because the aerosol system is nonlinear, the individual contributions depend on the prescribed sequence of experiments, while their sum recovers the complete charge-related CCN response in each regime.

Charge-dependent coagulation is the largest individual contribution in both environments (Fig. 3). It increases $N_{\mathrm{CCN},0.2}$ at 120 h by $5.80\,\%$ in the polluted regime and by $5.27\,\%$ in the clean regime. Charge-enhanced condensation contributes only $0.019\,\%$ and $0.00162\,\%$, respectively, and is therefore negligible in both environments. The neutral-kernel controls reproduce their corresponding neutral baselines to numerical precision, confirming that the coagulation increment arises from the charge-dependent collision kernel rather than from the numerical expansion of the population across charge states.

The contribution of ion-induced nucleation is strongly regime dependent. In the polluted regime, it increases $N_{\mathrm{CCN},0.2}$ by only $0.00139\,\%$. Ion-induced nucleation and charge-enhanced condensation contribute approximately $0.020\,\%$, making the

https://doi.org/10.5194/egusphere-2026-5224
Preprint. Discussion started: 28 September 2026

coagulation increment almost 300 times larger than the other two increments combined. Consequently, the complete polluted response of $5.82\,\%$ is attributable almost entirely to charge-dependent coagulation. The negligible CCN response from ion-induced production is consistent with global CLOUD-constrained modelling, which found limited present-day CCN sensitivity to changes in ion-induced particle production (Dunne et al., 2016). The negligible polluted ion-induced contribution results from the strong pre-existing aerosol sink. The polluted background provides a large surface area for ion–aerosol attachment, which rapidly removes positive and negative small ions from the gas phase (Fig. A2). The concentration of negative ions available to initiate the ion-induced nucleation pathway therefore remains low. The applied ion-induced formation rate reaches a maximum of only $6.9\times10^{-3}\,\mathrm{cm^{-3}\,s^{-1}}$, whereas the neutral H_2SO_4–DMA formation rate reaches values of order $10^{1}\,\mathrm{cm^{-3}\,s^{-1}}$ during the NPF bursts. Even at its maximum, the ion-induced pathway is therefore more than three orders of magnitude weaker than the neutral pathway. Under these high-sink conditions of the polluted regime, ion-induced nucleation produces too few additional particles to generate a measurable CCN response.

Ion-induced nucleation is considerably more important in the clean regime, where it contributes $3.60\,\%$ to $N_{\mathrm{CCN},0.2}$ at 120 h. The lower pre-existing aerosol sink reduces the scavenging of ions, nucleating clusters, and newly formed particles, while the HOM nucleation mechanism supports an efficient ion-induced production pathway. However, charge-dependent coagulation remains the largest individual contribution, providing $5.27\,\%$ compared with $3.60\,\%$ from ion-induced nucleation. These two processes explain almost all of the $8.87\,\%$ CCN enhancement in the clean regime. The very small condensation increment shows that the clean regime CCN response does not result directly from electrostatically enhanced vapour uptake.

The process attribution shows a common survival pathway and a regime-dependent production pathway. Ion-induced nucleation contributes substantially to CCN only in the clean regime, whereas charge-dependent coagulation produces a comparable CCN enhancement in both environments. The latter acts throughout the existing aerosol population by changing which charged particle pairs collide, which particles are removed, and how particle volume is redistributed among size classes. Charge-dependent coagulation is therefore the only substantial charge-related CCN pathway shared by both the polluted and clean regimes, while ion-induced production provides an additional clean-regime contribution.

https://doi.org/10.5194/egusphere-2026-5224
Preprint. Discussion started: 28 September 2026

3.3 Charge-dependent coagulation as the source of the response

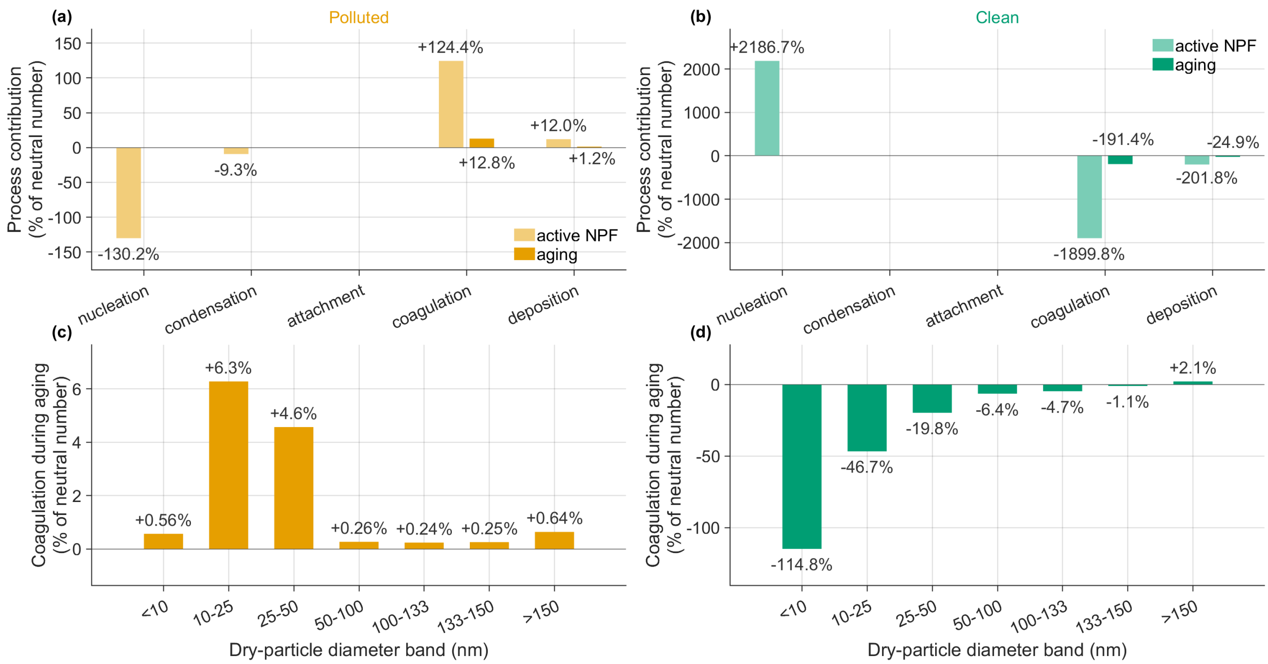

Figure 4. Contributions of nucleation, condensation, ion–aerosol attachment, coagulation, and deposition to the total particle-number difference between the charged and neutral cases for (a) polluted regime (C2c–C1) and (b) clean regime (B2c–B1), shown separately for active NPF (0–72 h) and aging (72–120 h). Aging-period coagulation contribution separated by particle-size range for the (c) polluted and (d) clean regimes.

365 Figure 4 shows the mechanistic attribution of the charge-induced particle-number response. Following the identification of charge-dependent coagulation as the largest contribution to the CCN response in Fig. 3, this analysis shows how coagulation interacts with nucleation and particle removal to produce the contrasting total-number responses in Fig. 2. The attribution closes to numerical precision, with maximum relative closure errors below 10^{-8}. Individual contributions represent cumulative production or removal normalised by the corresponding neutral particle number. They are particularly large in the clean regime
370 and should be interpreted together because substantial cancellation occurs between contributions of opposite sign.

During active NPF in the polluted regime, large nucleation and coagulation contributions oppose one another (Fig. 4a). Relative to C1, the integrated nucleation contribution in C2c is $-130.2\,\%$, while the coagulation contribution is $+124.4\,\%$. Condensation contributes $-9.3\,\%$, deposition contributes $+12.0\,\%$, and the direct contribution from ion–aerosol attachment is negligible. These terms sum to approximately $-3.1\,\%$, consistent with the $-3.07\,\%$ difference in total particle number
375 at 72 h. The positive coagulation contribution does not mean that coagulation creates particles. Instead, it means that the charge-resolved case experiences a smaller cumulative net particle-number loss through coagulation than the neutral case.

https://doi.org/10.5194/egusphere-2026-5224
Preprint. Discussion started: 28 September 2026

Nucleation contributes negatively in the polluted regime even though C1 and C2c use the same neutral H_2SO_4–DMA nucleation parameterisation. Charge-dependent coagulation modifies the evolving particle size distribution and hence the condensation sink for sulfuric-acid vapour. This changes the vapour concentration available for subsequent neutral nucleation bursts. The nucleation difference is therefore primarily an indirect response to the modified aerosol population rather than a direct electrical modification of the neutral nucleation. The ion-induced contribution remains negligible under the polluted, high-sink conditions as described in Sect. 3.2.

The clean-regime attribution follows a different pattern (Fig. 4b). During active NPF, nucleation contributes $+2186.7\,\%$ relative to B1, reflecting the strong additional ion-induced production in B2c. Most of this gross particle production is offset by a $-1899.8\,\%$ coagulation contribution and a $-201.8\,\%$ deposition contribution. Condensation and attachment make negligible direct contributions to total number. The remaining balance is approximately $+85\,\%$, consistent with the $+84.75\,\%$ total number enhancement at 72 h. Thus, the clean regime produces many additional particles, but coagulation and deposition remove most of them before the end of active NPF.

The aging-period attribution further distinguish the two environments. With nucleation switched off, the polluted response is controlled by positive coagulation and deposition contributions of $+12.8\,\%$ and $+1.2\,\%$, respectively. These contributions drive the reversal from a particle-number deficit at 72 h to a surplus at 120 h. In the clean regime, coagulation contributes $-191.4\,\%$ during aging and deposition contributes $-24.9\,\%$. These additional losses remove much of the large particle-number excess produced during active NPF, reducing $\Delta N_{\mathrm{total}}$ from $+84.75\,\%$ at 72 h to $+17.81\,\%$ at 120 h. The positive CCN response therefore does not require a positive charge-related contribution to total particle number.

The size-resolved aging contributions show why the particle-number response differs between the polluted and clean regimes (Fig. 4c,d). In the polluted regime, the coagulation contribution is positive in every diagnosed size band. The largest contributions occur at $10-25$ nm and $25-50$ nm, with values of $+6.3\%$ and $+4.6\%$, respectively. Smaller positive contributions extend through $50-100$, $100-133$, $133-150$, and >150 nm. The charged collision kernel therefore reduces the net loss of particles across the polluted size distribution, including particles approaching and exceeding the approximately 95 nm activation diameter at $0.2\,\%$ supersaturation. In the clean regime, charge-dependent coagulation produces strong net removal from the smaller size bands. Its contributions are $-114.8\,\%$ below 10 nm, $-46.7\,\%$ at 10–25 nm, and $-19.8\,\%$ at 25–50 nm. The negative contribution weakens progressively with increasing diameter, reaching $-6.4\,\%$ at 50–100 nm, $-4.7\,\%$ at 100–133 nm, and $-1.1\,\%$ at 133–150 nm. Above 150 nm, however, the contribution becomes positive at $+2.1\,\%$. Charge-dependent collisions therefore remove numerous small particles in this regime while transferring aerosol volume towards the largest size range.

The requirement for a charge-dependent collision kernel was tested using the neutral-kernel controls C2-NK and B2-NK. These cases retain ion production, ion–aerosol attachment, and the charge-resolved population, but apply the neutral Brownian collision kernel to every particle pair. Both controls reproduce their corresponding neutral baselines to numerical precision, with differences in total particle number and CCN remaining below the predefined $0.1\,\%$ acceptance threshold. Ion production, attachment, and movement between charge states therefore do not independently generate the coagulation response. A charge-dependent collision kernel is required.

https://doi.org/10.5194/egusphere-2026-5224
Preprint. Discussion started: 28 September 2026

Fig. 4 shows that charge-dependent coagulation enhances CCN through different particle-number pathways in the two environments. In the polluted regime, it primarily reduces cumulative particle loss and preserves particles across the growing size distribution. In the clean regime, it intensifies the scavenging of the numerous particles produced by ion-induced nucleation but transfers part of their aerosol volume into particles larger than 150 nm. The sign of the total-number contribution therefore cannot be used to infer the sign of the CCN response. In both regimes, the charge-dependent collision kernel changes the survival and redistribution of aerosol material into cloud-active size ranges, producing a positive CCN response despite opposing changes in total particle number.

3.4 Robustness and sensitivity

3.4.1 Sensitivity to the ion-pair production rate

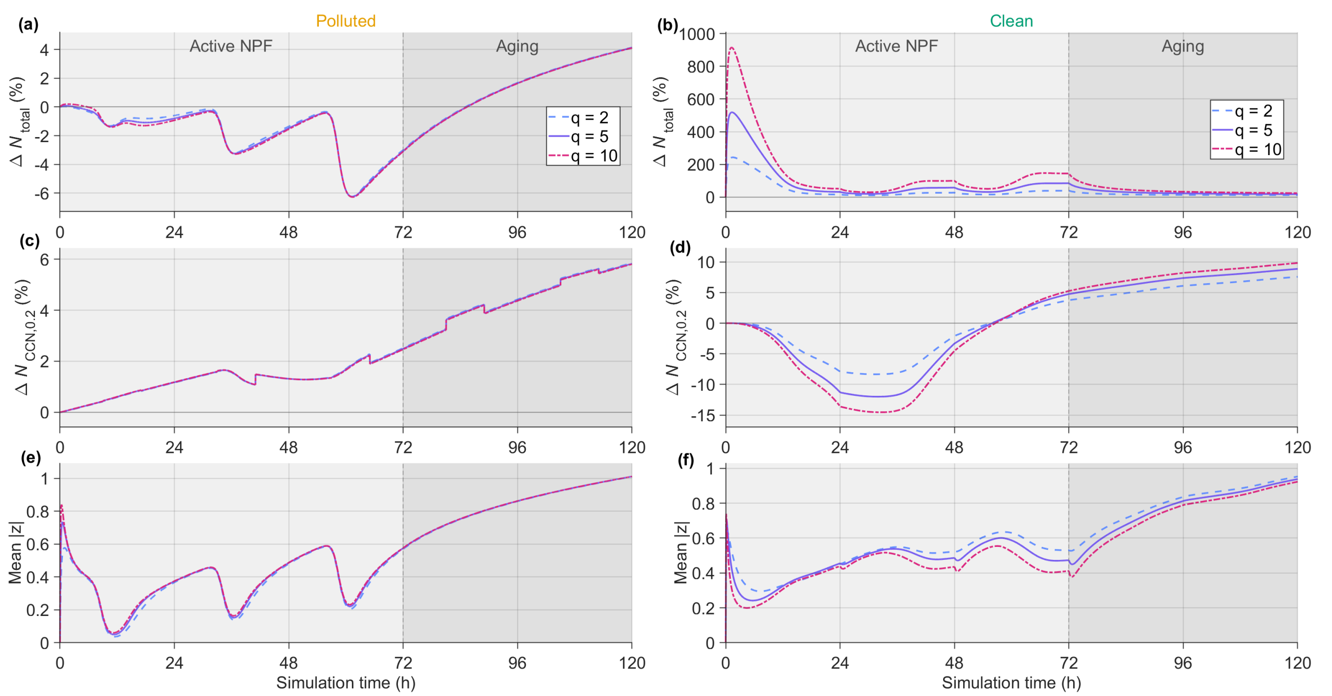

Figure 5. Relative difference in total particle number, $\Delta N_{\mathrm{total}}$, for (a) C2c relative to C1 in the polluted regime and (b) B2c relative to B1 in the clean regime; under varying ion-pair production rate, $q = 2$, 5, and 10 ion pairs $\mathrm{cm^{-3}\,s^{-1}}$. Relative difference in $N_{\mathrm{CCN,0.2}}$ for (c) C2c relative to C1 and (d) B2c relative to B1, under varying q; and mean absolute particle charge, $\langle |z| \rangle$, in (e) C2c and (f) B2c. Light- and dark-grey shading indicate active NPF and aging, respectively, and the dashed line marks the end of NPF at 72 h.

To determine whether the simulated response depends strongly on the prescribed small-ion source, the charge-resolved cases were repeated using ion-pair production rates of $q = 2$, 5, and 10 ion pairs $\mathrm{cm^{-3}\,s^{-1}}$. All meteorological inputs, vapour-production fields, background aerosol distributions, initial conditions, and microphysical settings were the same. The resulting particle-number and CCN responses are shown in Fig. 5.

The polluted-regime response is almost independent of q (Fig. 5a,c). The trajectories of ΔN_{total} and $\Delta N_{\text{CCN},0.2}$ are nearly identical across the tested q values throughout active NPF and aging. At 120 h, all three simulations produce an enhancement of approximately $4.1\,\%$ in total particle number and $5.8\,\%$ in $N_{\text{CCN},0.2}$. Increasing the ion-pair production rate by a factor of five therefore has almost no influence on the final polluted particle-number or CCN response.

The weak polluted sensitivity results from the strong pre-existing aerosol sink. Most newly produced small ions are rapidly removed by ion–aerosol attachment, while ion-induced nucleation remains negligible (Sect. 3.2). Consequently, changes in q primarily alter the rate at which the aerosol approaches its charge distribution rather than the number of new particles entering the system. Differences in $\langle |z| \rangle$ (Fig. 5e) are visible immediately after initialisation and around the repeated NPF bursts, but subsequently become small. During aging, all three polluted simulations approach $\langle |z| \rangle \approx 1$ by 120 h.

The clean regime is substantially more sensitive to q during active NPF because ion-induced nucleation provides an important particle-production pathway (Fig. 5b). The initial enhancement in N_{total} increases from approximately $250\,\%$ at $q = 2$ to more than $900\,\%$ at $q = 10$. Subsequent NPF cycles produce the same ordering, with the largest particle-number enhancement occurring at the highest ion-pair production rate. At 72 h, ΔN_{total} ranges from approximately $35\,\%$ at $q = 2$ to approximately $150\,\%$ at $q = 10$, with the baseline $q = 5$ simulation giving $84.75\,\%$. However, the particle-number response becomes much less sensitive to q during aging. Once nucleation is switched off, coagulation and deposition remove a large fraction of the additional small particles generated at higher q. By 120 h, the clean ΔN_{total} values have converged to a much narrower positive range of approximately 12–22 %. The clean particle-number response is therefore strongly sensitive to ion production during active NPF but much less sensitive after 48 h of post-NPF processing.

The clean CCN response further demonstrates that increased particle production does not translate directly into an immediate CCN enhancement (Fig. 5d). During the first two NPF cycles, $\Delta N_{\text{CCN},0.2}$ becomes negative, and the magnitude of this temporary deficit increases with q. The minimum response ranges from approximately $-8\,\%$ at $q = 2$ to approximately $-15\,\%$ at $q = 10$. Higher ion production creates more small particles, but these particles also increase competition for condensable vapour and undergo stronger coagulation scavenging. Consequently, fewer particles initially reach the activation size even though the total particle number is much larger. The sign of the clean CCN response reverses before the end of active NPF and remains positive throughout aging. At 120 h, $\Delta N_{\text{CCN},0.2}$ ranges from approximately $+7.5\,\%$ at $q = 2$ to approximately $+10\,\%$ at $q = 10$, with the $q = 5$ case producing $+8.87\,\%$. Thus, a fivefold change in ion production causes very large differences in the number of newly formed particles but changes the final CCN response by only a few percentage points. Post-formation survival and size redistribution strongly damp the sensitivity of CCN to ion-induced particle production.

Differences in the clean mean absolute charge are small relative to the differences in particle number (Fig. 5f). A higher value of q increases the supply of small ions, but it also produces a larger population of newly formed particles over which those charges are distributed. The ordering of $\langle |z| \rangle$ therefore does not follow a simple monotonic relationship with q. By 120 h, all three simulations approach values between approximately 0.9 and 1.0.

The sensitivity experiments demonstrate that the results are robust across the tested ion-production range. The polluted CCN response is effectively independent of q, consistent with its attribution to charge-dependent coagulation rather than ion-induced production. The clean regime retains a clear dependence of particle formation on q, but the corresponding CCN sensitivity is much weaker because most additional particles are removed before reaching cloud-active sizes. In both regimes, $N_{\mathrm{CCN},0.2}$ is enhanced over the neutral case at 120 h for every tested value of q.

3.4.2 Numerical robustness

The resolved size–charge distributions remain centred close to $z = 0$ in both the polluted and clean regimes at 72 and 120 h (Fig. A3). Positive and negative charge states are populated on either side of the neutral state, while the mean net particle charge, $\langle z \rangle$, remains close to zero. This is distinct from the mean absolute charge, $\langle |z| \rangle$, which remains finite because a substantial fraction of the aerosol population is charged. The simulations therefore represent approximately charge-balanced bipolar aerosol populations rather than predominantly neutral populations.

The charge distributions decay strongly before reaching the limits of the resolved grid at $z = -20$ and $z = +20$. The charge-boundary population and attachment-boundary fraction remain at least five orders of magnitude below their 10^{-4} reference value throughout both simulations (Fig. A4a,b). Similarly, the fraction associated with coagulation charge overflow remains at least four orders of magnitude below its 10^{-3} reference value (Fig. A4c). The clean-regime boundary fractions are generally several additional orders of magnitude smaller than those in the polluted regime. The simulated particle-number and CCN responses are therefore not controlled by truncation at the imposed charge-state boundaries.

The maximum coagulation-loss Courant number remains below unity in both regimes (Fig. A4d). Its maximum value is approximately 0.81 in the polluted simulation and 0.62 in the clean simulation, with the largest values occurring during the strongest NPF periods. Coagulation is additionally integrated using a semi-implicit solver, which limits sensitivity to rapid changes in particle concentration. The charge-boundary diagnostics, coagulation-overflow diagnostics, and Courant numbers therefore demonstrate that the reported particle number and CCN responses are not numerical artefacts of the charge grid or coagulation integration.

4 Discussion

4.1 Charge regulates aerosol survival

Across both regimes, the simulations show a common route by which aerosol charge influences the population that reaches CCN-active sizes. For the CCN response, the dominant control is not simply the production of additional particles by ion-induced nucleation, but the modification of particle survival and size redistribution by charge-dependent coagulation. Enhanced collisions between oppositely charged particles and suppressed collisions between similarly charged particles alter the evolution of the size distribution over several days. The resulting changes in particle number and size also modify the condensation sink, providing a secondary vapour-mediated feedback on subsequent particle growth and nucleation.

https://doi.org/10.5194/egusphere-2026-5224
Preprint. Discussion started: 28 September 2026

This behaviour produces two features that are not apparent from total particle number alone. First, the number and CCN responses can have different signs: charging can reduce total particle number while increasing CCN because losses and gains occur in different parts of the size distribution. Second, the response is stage dependent. During active NPF, charge-enhanced collisions can remove small particles and reduce total number, whereas during subsequent aging, the redistribution of surviving particles and the associated vapour feedback can increase the abundance at larger sizes. The CCN response remains positive despite these changes in the sign of the total-number response. Total particle number alone is therefore insufficient to diagnose the cloud-relevant effect of charge; the evolution of the size distribution and the fraction of particles reaching activation sizes must also be considered.

The neutral-kernel control isolates the role of charge-dependent collision physics, while the process-contribution analysis shows that ion-induced nucleation and charge-related changes in condensation make substantially smaller direct contributions to the final CCN response. In the clean regime, ion-induced nucleation remains important for supplying newly formed particles to the system. Their subsequent fate is determined primarily by the survival pathway, in which charge-dependent coagulation controls how much of that newly formed population is removed at small sizes and how much is redistributed toward larger sizes. We therefore describe the mechanism as *charge-regulated aerosol survival*: charge modifies which particles persist and reach CCN-relevant sizes rather than acting only through changes in the initial particle-production rate. A schematic summary of this mechanism is shown in Fig. 6.

https://doi.org/10.5194/egusphere-2026-5224
Preprint. Discussion started: 28 September 2026

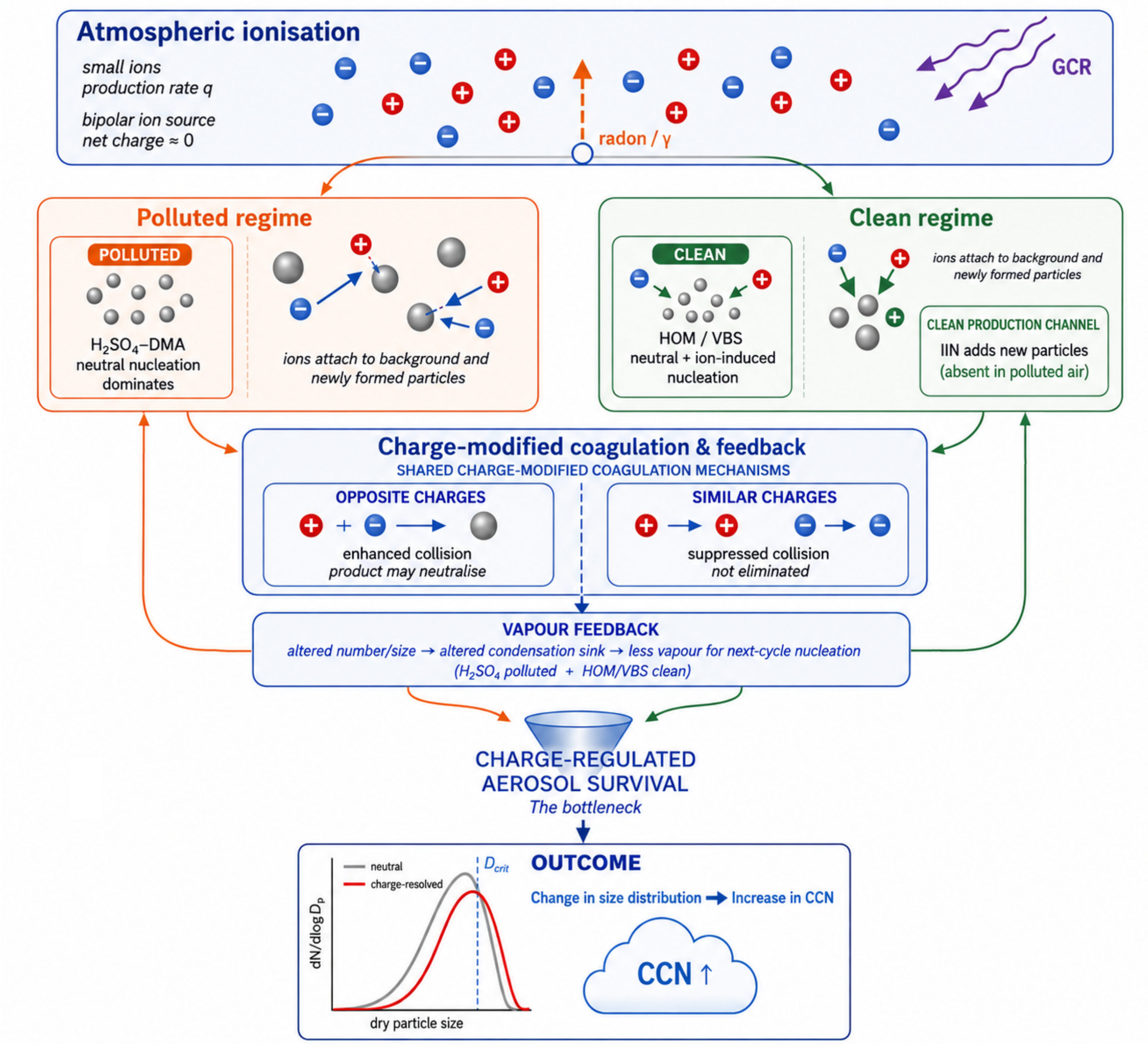

Figure 6. Schematic representation of charge-regulated aerosol survival across the polluted and clean regimes. Atmospheric ionisation establishes a bipolar small-ion population that charges background and newly formed particles. The particle-formation pathway is regime dependent: neutral H_2SO_4–DMA nucleation dominates in the polluted regime, whereas ion-induced nucleation provides an additional particle source in the clean regime. In both environments, charge-dependent coagulation modifies particle survival and redistribution through enhanced collisions between oppositely charged particles and suppressed collisions between similarly charged particles. The resulting changes in particle number and size alter the condensation sink and hence vapour availability, providing feedback to subsequent nucleation and growth. These regime-specific pathways converge on a common charge-regulated aerosol-survival bottleneck that determines the fraction of particles able to grow toward the regime-dependent critical diameter for CCN activation.

https://doi.org/10.5194/egusphere-2026-5224
Preprint. Discussion started: 28 September 2026

4.2 A mechanism that persists across contrasting regimes

The two regimes were selected to represent strongly contrasting boundary-layer aerosol conditions. The polluted regime combines H_2SO_4-DMA nucleation with a high condensation sink, high background aerosol loading and strong ion depletion. The clean boreal regime instead combines biogenic HOM-driven nucleation and volatility-resolved organic growth with a substantially lower condensation sink and greater small-ion availability. The regimes also differ in aerosol loading, composition, hygroscopicity and the vapours controlling particle formation and growth. Despite these differences, charge-dependent coagulation increases $N_{\mathrm{CCN},0.2}$ by a similar amount in both regimes: $+5.8\,\%$ in polluted air and $+5.3\,\%$ in clean air. The similar response in these contrasting environments suggests that the survival mechanism is not limited to one chemical or pollution regime.

The underlying particle-number responses are, however, very different between the two regimes. In the polluted regime, ion-induced nucleation is weak and the CCN response arises primarily from charge-dependent redistribution of the existing and newly formed particle population. In the clean regime, ion-induced nucleation provides a substantial additional source of small particles. Most of this enhanced production does not translate directly into an equivalent increase in CCN, because the newly formed particles remain subject to strong size-dependent losses during their growth. Charge-dependent coagulation therefore acts as a survival filter, removing part of the enhanced small-particle population while redistributing surviving particle number toward larger sizes.

The same broad survival mechanism consequently produces a positive CCN response in both regimes even though the corresponding total-number responses differ. In the polluted regime, charge primarily modifies the survival and growth of a population formed predominantly through neutral nucleation. In the clean regime, charge additionally enhances particle production through ion-induced nucleation, but the eventual CCN yield is still controlled mainly by the subsequent survival of those particles. The clean simulation therefore illustrates an important distinction between particle production and CCN production: a large charge-induced change in the number of newly formed particles does not imply a proportionally large change in the number that ultimately reaches cloud-active sizes.

The importance of this distinction becomes particularly clear during the aging period. The clean-regime CCN enhancement persists after the active nucleation period, even as the small-particle population is progressively processed. Charge-induced changes in the size distribution also modify the condensation sink and hence the vapour available for later growth. This feedback differs chemically between the two regimes, involving H_2SO_4-related growth in the polluted case and HOM/VBS vapours in the clean case, but in both cases it links earlier charge-dependent changes in particle number and size to the subsequent evolution of the CCN population.

4.3 Relation to prior ion-aerosol-cloud mechanisms

Previous assessments of ionisation effects on CCN have focused mainly on the particle-production pathway, particularly whether changes in ion-pair production alter ion-induced nucleation sufficiently for additional particles to survive to cloud-active sizes. Global and chamber-constrained studies have shown that this pathway is strongly limited by the loss of newly formed particles before they reach CCN sizes (Pierce and Adams, 2009; Dunne et al., 2016). Our results are consistent with

https://doi.org/10.5194/egusphere-2026-5224
Preprint. Discussion started: 28 September 2026

this interpretation but add an important distinction between ion-induced particle production and charge-dependent particle survival.

In the clean regime, ion-induced nucleation responds strongly to the ion source and can substantially alter the abundance of newly formed particles. However, the corresponding CCN response is much smaller because only a fraction of that additional population survives the transition from nucleation sizes to cloud-active sizes. The simulations show that charge-dependent coagulation is central to this filtering process. A framework based only on changes in the nucleation rate can therefore miss an important part of the ion-aerosol interaction: charge can influence CCN even when its effect on nucleation is small, because the charge carried by the aerosol modifies collisions throughout the subsequent particle-evolution pathway.

This distinction also refines the interpretation of the cosmic-ray-cloud hypothesis (Svensmark and Friis-Christensen, 1997; Carslaw et al., 2002). Across the ion-production rates examined here, changes in the ion source have a much larger effect on small-particle production than on CCN. This behaviour is particularly evident in the clean regime, where ion-induced nucleation responds strongly to the ion source but the resulting change in CCN is small. The survival bottleneck therefore reduces the propagation of ion-production variability from nucleation to CCN.

At the same time, the charge-dependent coagulation effect does not require a large temporal perturbation in the ion source. Ambient ion production continually maintains a bipolar population of small ions, while ion attachment and recombination regulate the aerosol charge distribution. The mechanism identified here should therefore be interpreted primarily as a consequence of the persistent charged state of atmospheric aerosol rather than as evidence for a large CCN response to short-term variability in cosmic-ray or other ionisation sources.

The mechanism considered here is also distinct from cloud-edge electrification, in which charge accumulated near cloud boundaries can modify aerosol scavenging, droplet interactions or activation locally (Nicoll and Harrison, 2016; Tinsley, 2008). Charge-regulated aerosol survival operates earlier in the aerosol life cycle, during the multi-hour to multi-day evolution of the particle population before cloud activation. These processes are not mutually exclusive. Charge-dependent aerosol evolution can modify the population arriving at cloud base, after which cloud-scale electrical processes may further influence activation or collection.

4.4 Limitations and outlook

The present framework is zero dimensional and assumes a well-mixed air parcel. It therefore omits dilution, entrainment, spatial gradients and advection. In the atmosphere, air-mass exchange over several days could modify the aging phase, during which the size distribution continues to evolve and the CCN enhancement develops. The active NPF period is less exposed to this limitation, but the magnitude and persistence of the multi-day response should ultimately be tested in a spatially resolved framework.

Particle growth is represented using chemistry appropriate to each regime, with sulfuric-acid-amine chemistry in the polluted case and volatility-resolved organic vapours in the clean case. Charge acts primarily on the evolving particle population rather than on a specific condensable vapour, but the resulting survival pathway is coupled to growth. Different precursor mixtures, oxidation chemistry and vapour-production histories could therefore alter both the growth timescale and the strength of the

https://doi.org/10.5194/egusphere-2026-5224
Preprint. Discussion started: 28 September 2026

condensation-sink feedback. The present two-regime comparison demonstrates that the mechanism persists under strongly contrasting conditions, but it does not define its magnitude for all atmospheric environments.

The simulations also represent a finite period of repeated NPF and aging rather than the full life cycle of an atmospheric aerosol population. Longer simulations and observationally constrained air-mass histories would be useful for determining how long the charge-induced redistribution persists and whether it remains detectable after additional mixing, deposition and chemical aging.

CCN are diagnosed from the dry particle-size distribution using κ-Köhler theory rather than by explicitly simulating cloud activation. The present study therefore establishes a response in CCN abundance, not a direct response in cloud-droplet number, liquid-water path, precipitation or radiative forcing. Charge-dependent activation itself is not included because the electro-Köhler correction is negligible for the charge states represented at CCN-relevant sizes. A natural next step is therefore to couple the charge-resolved aerosol population to spatially resolved and cloud-resolving models in order to determine how much of the diagnosed CCN response propagates to cloud-droplet number and cloud radiative properties.

5 Conclusion

Using matched neutral and charge-resolved simulations with the ELSA-ICAM model, we show that electrical charging under ordinary atmospheric ionisation can modify the pathway from new particle formation to cloud condensation nuclei. The response persists across two strongly contrasting atmospheric regimes, although the relative roles of nucleation, coagulation and vapour feedback differ between them.

In the polluted regime, bipolar charging reduces total particle number by $3.07\,\%$ at $72\,\mathrm{h}$ while increasing $N_{\mathrm{CCN},0.2}$ by $2.49\,\%$. By $120\,\mathrm{h}$, the total-number response reverses to $+4.12\,\%$ and the CCN response increases to $+5.83\,\%$. The neutral-kernel control and mechanistic attribution identify charge-dependent coagulation as the dominant mechanism responsible for this response. The opposite signs of the number and CCN changes demonstrate that charge does not simply increase or decrease the aerosol population uniformly. Instead, it redistributes particle number across the size distribution and changes the fraction that survives to cloud-active sizes.

The clean regime follows a different particle-production pathway. Ion-induced nucleation produces a substantial additional population of small particles, but much of this enhanced production is removed before reaching CCN-active sizes. At $120\,\mathrm{h}$, the complete charge-resolved case increases $N_{\mathrm{CCN},0.2}$ by $8.87\,\%$ relative to the neutral case. Charge-dependent coagulation provides the largest individual contribution, $+5.27\,\%$, while ion-induced nucleation contributes an additional $+3.60\,\%$. Charge-enhanced condensation is negligible. Thus, despite the much larger effect of ion-induced nucleation on particle production, charge-dependent coagulation remains the dominant shared contribution to CCN in both regimes.

The central result is therefore a distinction between particle production and CCN production. Ion-induced nucleation can strongly affect the number of particles formed, particularly under clean conditions, but the eventual CCN yield is governed mainly by the survival of those particles during subsequent growth and coagulation. Charge-dependent coagulation provides a common microphysical control on that survival in both regimes. Its effect can persist into the aging period and can be reinforced by changes in the condensation sink and vapour availability generated by the earlier redistribution of particle number and size.

The simulations further show that the CCN response is much less sensitive to the ion-production rate than the small-particle population itself. This implies that variability in ionisation does not propagate directly from nucleation to CCN because the intervening survival bottleneck strongly filters the additional particle production. The mechanism identified here is therefore better viewed as a consequence of persistent bipolar aerosol charging maintained by ambient ionisation than as a direct CCN response to variations in the ion source.

We term this mechanism *charge-regulated aerosol survival*. It is distinct from both ion-induced particle production and electrical effects occurring at cloud boundaries. The polluted and clean simulations show that it remains relevant under strongly contrasting boundary-layer aerosol conditions and can produce several-percent changes in CCN even when the corresponding particle-number responses differ substantially. Because charge-resolved coagulation is not represented in most conventional aerosol-cloud models, testing this mechanism in spatially resolved aerosol and cloud simulations is an important next step. Such simulations will determine whether the CCN response identified here propagates to cloud-droplet number and ultimately to cloud radiative properties.

Appendix A: Supplementary figures

The following figures document the two-regime precursor forcing and particle response, the small-ion budget, the joint size–charge distributions, and the numerical diagnostics referenced in the main text.

A1 Two-regime forcing, nucleation, and number response

Figure A1 compares the polluted and clean simulations under the matched 120 h protocol. The upper panels show the prescribed precursor production and the resulting gas-phase concentration: sulfuric acid in the polluted regime and highly oxygenated organic molecules (HOMs) in the clean regime. The middle panels separate the neutral nucleation rate, J_n, from the total ion-induced rate, $J_i = J_{i,+} + J_{i,-}$. Ion-induced nucleation is negligible in the polluted regime but is a substantial production pathway in the clean regime. Consequently, the polluted C1 and C2c total-number responses remain very similar, whereas the clean B2c simulation maintains a larger particle number than B1. Precursor production and nucleation are switched off after 72 h, after which the existing aerosol population continues to evolve during post-NPF aging.

https://doi.org/10.5194/egusphere-2026-5224
Preprint. Discussion started: 28 September 2026

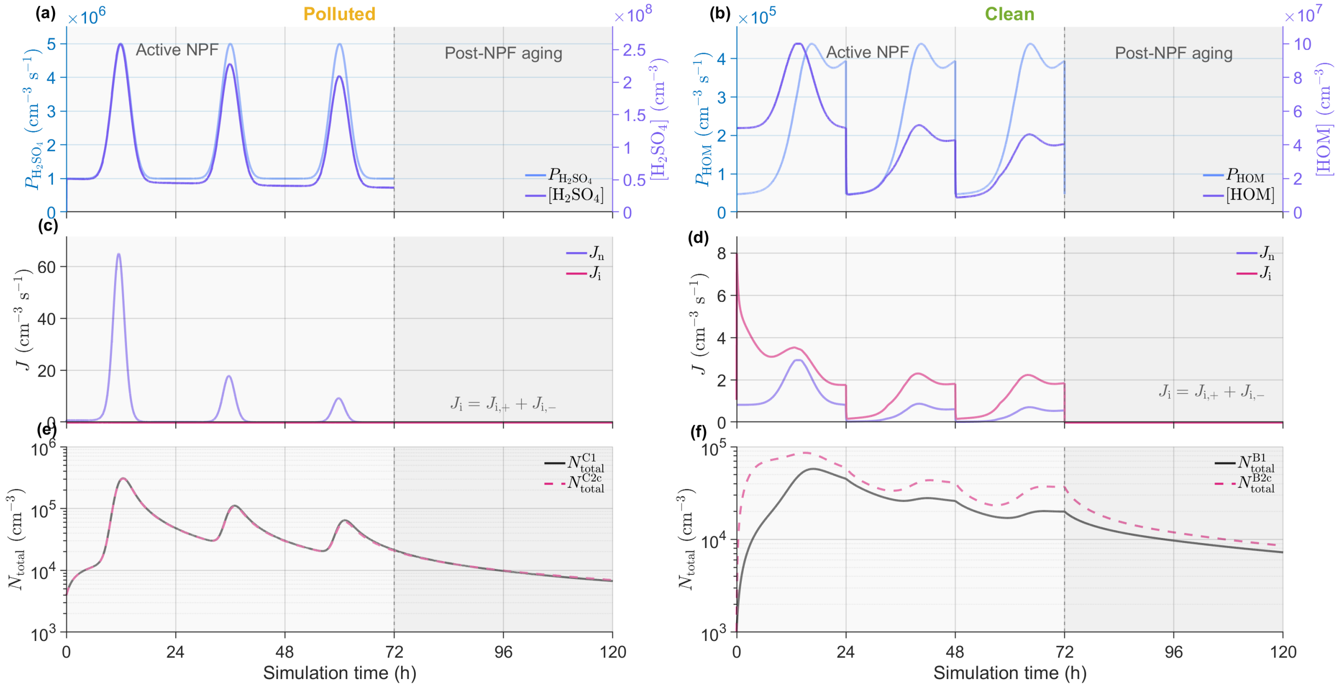

Figure A1. Two-regime forcing, nucleation, and total-number response. Panels (a,b) show precursor production and gas-phase concentration for the polluted regime [$P_{H_2SO_4}$ and [H_2SO_4]] and the clean regime [P_{HOM} and [HOM]], respectively. Panels (c,d) show the neutral nucleation rate, J_n, and the total ion-induced nucleation rate, $J_i = J_{i,+} + J_{i,-}$. Panels (e,f) compare the neutral and charge-resolved total particle numbers: N^{C1}_{total} and N^{C2c}_{total} for the polluted regime, and N^{B1}_{total} and N^{B2c}_{total} for the clean regime. Grey shading distinguishes active NPF (0–72 h) from post-NPF aging (72–120 h).

A2 Small-ion concentrations and budgets

Figure A2 shows the positive and negative small-ion concentrations, their relative imbalance, ϵ_n, and the per-polarity rate budgets. The budget terms are ion-pair production, q; ion–ion recombination, $\mathcal{R}_{rec}$; ion attachment to aerosol particles, $A^{\pm}$; and ion-induced nucleation, $J^{\pm}_{IIN}$. In the polluted regime, attachment balances almost all ion production, while recombination and ion-induced nucleation are small. In the clean regime, attachment and ion-induced nucleation jointly consume small ions during active NPF. The ion-induced nucleation terms vanish when NPF is switched off at 72 h. The close agreement between n^+ and n^- and the very small ϵ_n confirm that both simulations remain effectively bipolar and net-neutral.

https://doi.org/10.5194/egusphere-2026-5224
Preprint. Discussion started: 28 September 2026

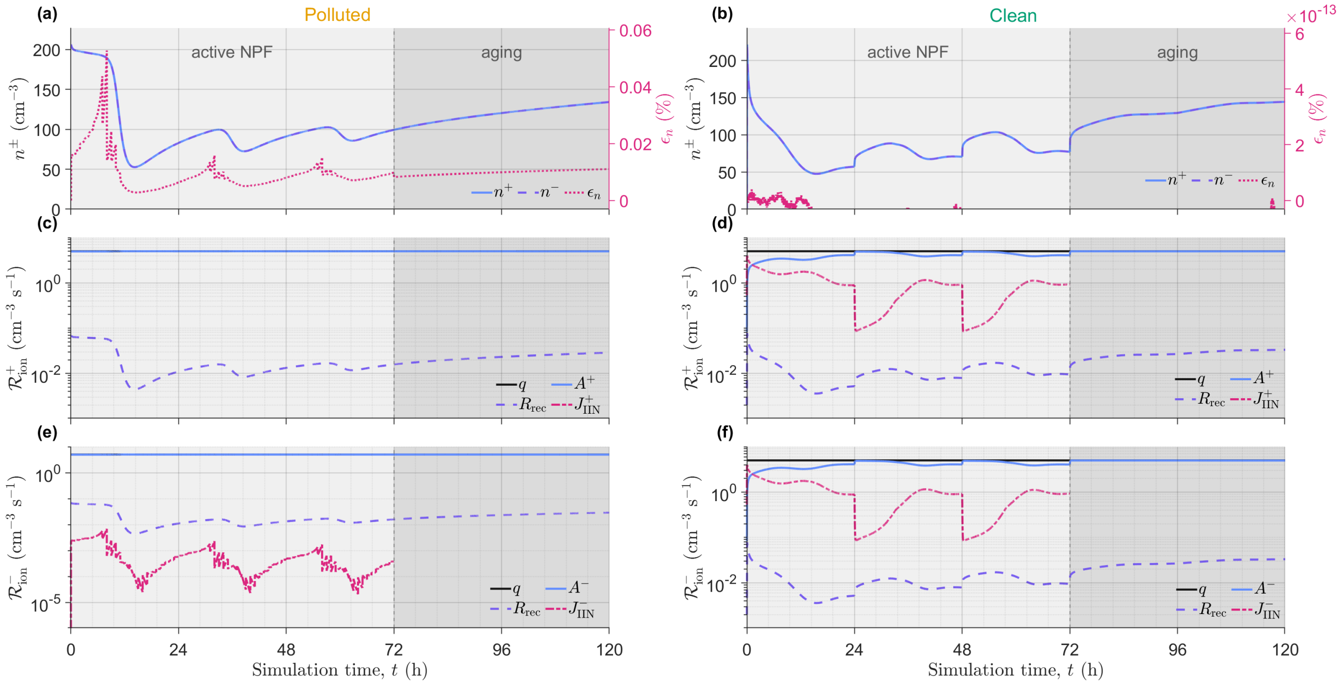

Figure A2. Small-ion concentrations and per-polarity budgets in the polluted (left) and clean (right) simulations. Panels (a,b) show the positive and negative small-ion concentrations, n^+ and n^-, and their relative imbalance, ϵ_n. Panels (c,d) show the positive-ion budget, and panels (e,f) show the negative-ion budget. The terms are ion-pair production, q; ion–ion recombination, $\mathcal{R}_{\rm rec}$; ion–aerosol attachment, $A^{\pm}$; and ion-induced nucleation, $J^{\pm}_{\rm IIN}$. Attachment dominates the polluted ion sink, whereas attachment and ion-induced nucleation jointly consume ions during active NPF in the clean regime. Grey shading distinguishes active NPF from post-NPF aging.

A3 Joint size–charge distributions

635 Figure A3 shows $\mathrm{d}N_z/\mathrm{d}\log_{10}D_p$ as a joint function of dry-particle diameter, D_p, and charge state, z, for the polluted and clean simulations at 72 and 120 h. The 72 h distributions represent the end of active NPF, whereas the 120 h distributions show the populations after 48 h of post-NPF aging. A common logarithmic vertical and colour scale permits direct comparison between regimes and times. In both regimes, the populated charge states remain well inside the finite $z = -20, \ldots, +20$ grid.

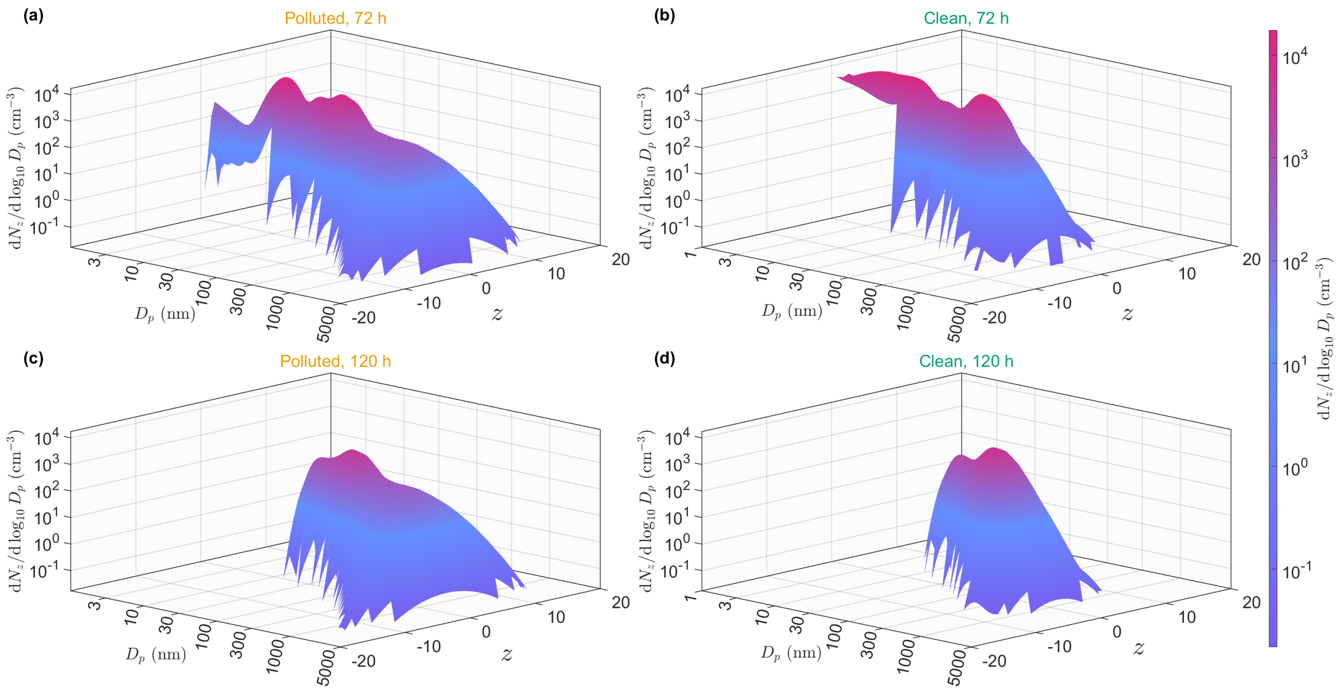

Figure A3. Joint particle size–charge distributions, $dN_z/d\log_{10} D_p$, for (a) the polluted simulation at 72 h, (b) the clean simulation at 72 h, (c) the polluted simulation at 120 h, and (d) the clean simulation at 120 h. The horizontal coordinates are dry-particle diameter, D_p, and integer charge state, z. All panels use the same logarithmic vertical and colour scales. The two times correspond to the end of active NPF and the end of the subsequent 48 h aging period, respectively.

A4 Numerical diagnostics

640 Figure A4 compares the charge-boundary fraction, f_{bnd}; the attachment-boundary fraction, $f_{\mathrm{att,bnd}}$; the coagulation charge-overflow fraction, $f_{\mathrm{coag},z}$; and the maximum coagulation-loss number, $\mathcal{C}_{\mathrm{coag,max}}$, in the final $q = 5\,\mathrm{cm}^{-3}\,\mathrm{s}^{-1}$ and $\Delta t = 15\,\mathrm{s}$ simulations.

All boundary and overflow fractions remain many orders of magnitude below their reference values. Their respective maxima in the polluted and clean simulations are 1.40×10^{-9} and 1.84×10^{-14} for f_{bnd}, 2.74×10^{-9} and 2.06×10^{-14} for $f_{\mathrm{att,bnd}}$,
645 and 5.43×10^{-7} and 2.01×10^{-11} for $f_{\mathrm{coag},z}$. The maximum coagulation-loss number also remains below unity, reaching 0.81 in the polluted simulation and 0.62 in the clean simulation.

These results confirm both charge-grid sufficiency and the numerical adequacy of the final matched simulations.

https://doi.org/10.5194/egusphere-2026-5224
Preprint. Discussion started: 28 September 2026

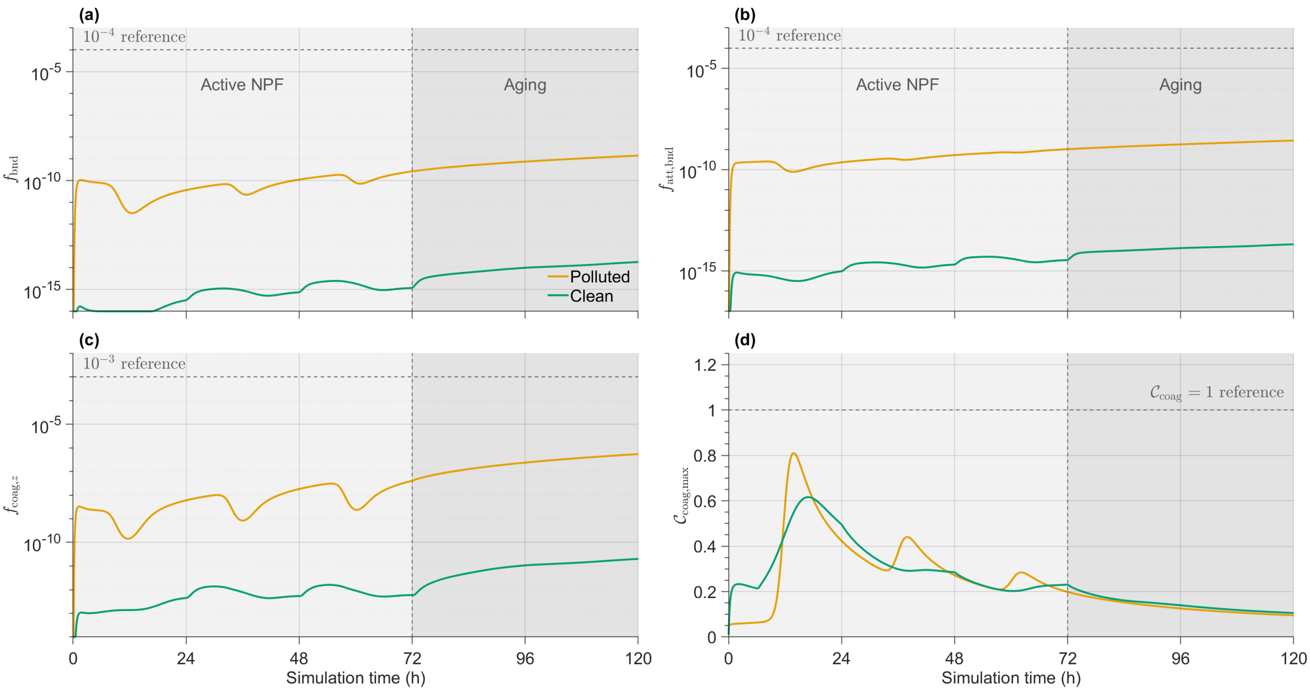

Figure A4. Numerical diagnostics for the polluted (orange) and clean (green) charge-resolved simulations. Panels show (a) the charge-boundary fraction, f_{bnd}; (b) the attachment-boundary fraction, $f_{\mathrm{att,bnd}}$; (c) the coagulation charge-overflow fraction, $f_{\mathrm{coag},z}$; and (d) the maximum coagulation-loss number, $\mathcal{C}_{\mathrm{coag,max}}$. The dashed horizontal lines are numerical reference values rather than physical thresholds. Boundary and overflow fractions remain far below their reference values, and $\mathcal{C}_{\mathrm{coag,max}} < 1$ in both final $\Delta t = 15\,\mathrm{s}$ simulations. Grey shading distinguishes active NPF from post-NPF aging.

Code and data availability

The processed model output and figure-reproduction data used in this study are available on Zenodo at https://doi.org/10.5281/zenodo.22163101. The ELSA-ICAM model code used to perform the simulations is available from the corresponding author upon reasonable request.

Author contribution

KG conceived the study and developed the charge-regulated aerosol survival hypothesis. KG designed the model approach, the charge-resolved framework and the matched-twin experimental design, with contributions from GS and SM. KG developed and extended the model code, performed all simulations, and carried out the formal analysis, with contributions from GS. SM prepared the observational constraint from the Delhi campaign and SMEAR data. KG, GS and SM validated the results. KG

https://doi.org/10.5194/egusphere-2026-5224
Preprint. Discussion started: 28 September 2026

produced the figures with input from all authors, and coordinated the project. GS wrote the original draft, with contributions from KG and SM. All authors contributed to the interpretation of the results and to reviewing and editing the manuscript.

Competing interests

The authors declare no competing interests.

Acknowledgements

The authors thank Prof. Ken Carslaw, University of Leeds, for valuable discussions and support during this work. This work was supported in part by the Natural Environment Research Council (NERC) through the Aerosol-MFR project (grant NE/X013901/1). No additional funding was received. OpenAI ChatGPT image-generation tools were used to assist with the graphical design of the schematic figures. All scientific content, labels, numerical results, and interpretations were specified and verified by the authors.

References

Abdul-Razzak, H. and Ghan, S. J.: A parameterization of aerosol activation, 2. Multiple aerosol types, J. Geophys. Res., 105, 6837–6844, https://doi.org/10.1029/1999JD901161, 2000.

Albrecht, B. A.: Aerosols, cloud microphysics, and fractional cloudiness, Science, 245, 1227–1230, https://doi.org/10.1126/science.245.4923.1227, 1989.

Bazilevskaya, G. A. et al.: Cosmic ray induced ion production in the atmosphere, Space Sci. Rev., 137, 149–173, https://doi.org/10.1007/s11214-008-9339-y, 2008.

Brattich, E., Serrano Castillo, E., Giulietti, F., Renard, J.-B., Tripathi, S. N., Ghosh, K., et al.: Measurements of aerosols and charged particles on the BEXUS18 stratospheric balloon, Ann. Geophys., 37, 389–403, https://doi.org/10.5194/angeo-37-389-2019, 2019.

Brean, J., Rowell, A., Beddows, D. C. S., Shi, Z., and Harrison, R. M.: Estimates of Future New Particle Formation under Different Emission Scenarios in Beijing, Environmental Science & Technology, 57, 4741–4750, https://doi.org/10.1021/acs.est.2c08348, pMID: 36930743, 2023.

Carslaw, K. S., Harrison, R. G., and Kirkby, J.: Cosmic rays, clouds, and climate, Science, 298, 1732–1737, https://doi.org/10.1126/science.1076964, 2002.

Carslaw, K. S. et al.: Large contribution of natural aerosols to uncertainty in indirect forcing, Nature, 503, 67–71, https://doi.org/10.1038/nature12674, 2013.

Deng, C., Cai, R., and Yan, C.: Formation and growth of sub-3 nm particles in megacities: impact of background aerosols, Faraday Discussions, 226, 348–363, https://doi.org/10.1039/D0FD00083C, 2021.

Dunne, E. M. et al.: Global atmospheric particle formation from CERN CLOUD measurements, Science, 354, 1119–1124, https://doi.org/10.1126/science.aaf2649, 2016.

Forster, P. et al.: The Earth's Energy Budget, Climate Feedbacks, and Climate Sensitivity, in: Climate Change 2021 (IPCC AR6 WG1), Cambridge University Press, https://doi.org/10.1017/9781009157896.009, 2021.

Ghosh, K., Tripathi, S. N., Joshi, M., Mayya, Y. S., Khan, A., and Sapra, B. K.: Modeling studies on coagulation of charged particles and comparison with experiments, J. Aerosol Sci., 105, 35–47, https://doi.org/10.1016/j.jaerosci.2016.11.019, 2017.

Ghosh, K., Tripathi, S. N., Joshi, M., Mayya, Y. S., Khan, A., and Sapra, B. K.: Effect of charge on aerosol microphysics of particles emitted from a hot wire generator: Theory and experiments, Aerosol Science and Technology, 55, 1084–1098, https://doi.org/10.1080/02786826.2021.1931011, 2021.

Ghosh, K., Sengupta, G., and Mishra, S.: How Microscale Flow and Vapor Transport Shape New Particle Formation and Growth, Environmental Science & Technology, https://doi.org/10.1021/acs.est.6c10206, 2026.

Gilbert, J. S. et al.: Charge measurements on particle fallout from a volcanic plume, Nature, 349, 598–600, https://doi.org/10.1038/349598a0, 1991.

Gordon, H. et al.: Causes and importance of new particle formation in the present-day and preindustrial atmospheres, J. Geophys. Res. Atmos., 122, 8739–8760, https://doi.org/10.1002/2017JD026844, 2017.

Grosvenor, D. P. et al.: Remote sensing of droplet number concentration in warm clouds: a review, Rev. Geophys., 56, 409–453, https://doi.org/10.1029/2017RG000593, 2018.

Harrison, R. G. and Carslaw, K. S.: Ion-aerosol-cloud processes in the lower atmosphere, Rev. Geophys., 41, 1012, https://doi.org/10.1029/2002RG000114, 2003.

Harrison, R. G. et al.: Self-charging of the Eyjafjallajökull volcanic ash plume, Environ. Res. Lett., 5, 024 004, https://doi.org/10.1088/1748-9326/5/2/024004, 2010.

Hirsikko, A. et al.: Atmospheric ions and nucleation: a review of observations, Atmos. Chem. Phys., 11, 767–798, https://doi.org/10.5194/acp-11-767-2011, 2011.

Hoppel, W. A. and Frick, G. M.: Ion-aerosol attachment coefficients and the steady-state charge distribution on aerosols in a bipolar environment, Aerosol Sci. Technol., 5, 1–21, https://doi.org/10.1080/02786828608959073, 1986.

Junninen, H., Lauri, A., Keronen, P., Aalto, P., Hiltunen, V., Hari, P., and Kulmala, M.: Smart-SMEAR: on-line data exploration and visualization tool for SMEAR stations, Boreal Environment Research, 14, 447–457, 2009.

Kerminen, V.-M. and Kulmala, M.: Analytical formulae connecting the “real” and the “apparent” nucleation rate and the nuclei number concentration for atmospheric nucleation events, Journal of Aerosol Science, 33, 609–622, https://doi.org/10.1016/S0021-8502(01)00194-X, 2002.

Kerminen, V.-M. et al.: Atmospheric new particle formation and growth: review of field observations, Environ. Res. Lett., 13, 103 003, https://doi.org/10.1088/1748-9326/aadf3c, 2018.

Kirkby, J. et al.: Role of sulphuric acid, ammonia and galactic cosmic rays in atmospheric aerosol nucleation, Nature, 476, 429–433, https://doi.org/10.1038/nature10343, 2011.

Kirkby, J. et al.: Ion-induced nucleation of pure biogenic particles, Nature, 533, 521–526, https://doi.org/10.1038/nature17953, 2016.

Laakso, L. et al.: Ultrafine particle scavenging coefficients and charge effects, Atmos. Environ., 36, 4093–4099, https://doi.org/10.1016/S1352-2310(02)00370-1, 2002.

Lehtinen, K. E., Dal Maso, M., Kulmala, M., and Kerminen, V.-M.: Estimating nucleation rates from apparent particle formation rates and vice versa: Revised formulation of the Kerminen–Kulmala equation, Journal of Aerosol Science, 38, 988–994, https://doi.org/https://doi.org/10.1016/j.jaerosci.2007.06.009, 2007.

Merikanto, J. et al.: Impact of nucleation on global CCN, Atmos. Chem. Phys., 9, 8601–8616, https://doi.org/10.5194/acp-9-8601-2009, 2009.

Mishra, S., Tripathi, S. N., Kanawade, V. P., et al.: Rapid night-time nanoparticle growth in Delhi driven by biomass-burning emissions, Nat. Geosci., 16, 224–230, https://doi.org/10.1038/s41561-023-01138-x, 2023.

Nicoll, K. A. and Harrison, R. G.: Stratiform cloud electrification: comparison of theory with multiple in-cloud measurements, Q. J. R. Meteorol. Soc., 142, 2679–2691, https://doi.org/10.1002/qj.2858, 2016.

Nicoll, K. A. et al.: Observations of Saharan dust layer electrification, Environ. Res. Lett., 6, 014 001, https://doi.org/10.1088/1748-9326/6/1/014001, 2011.

Petroff, A. and Zhang, L.: Development and validation of a size-resolved particle dry deposition scheme for application in aerosol transport models, Geoscientific Model Development, 3, 753–769, https://doi.org/10.5194/gmd-3-753-2010, 2010.

Petters, M. D. and Kreidenweis, S. M.: A single parameter representation of hygroscopic growth and CCN activity, Atmos. Chem. Phys., 7, 1961–1971, https://doi.org/10.5194/acp-7-1961-2007, 2007.

Pierce, J. R. and Adams, P. J.: Efficiency of cloud condensation nuclei formation from ultrafine particles, Atmospheric Chemistry and Physics, 7, 1367–1379, https://doi.org/10.5194/acp-7-1367-2007, 2007.

Pierce, J. R. and Adams, P. J.: Can cosmic rays affect cloud condensation nuclei by altering new particle formation rates?, Geophys. Res. Lett., 36, L09 820, https://doi.org/10.1029/2009GL037946, 2009.

https://doi.org/10.5194/egusphere-2026-5224
Preprint. Discussion started: 28 September 2026

Renard, J.-B., Tripathi, S. N., Michael, M., Rawal, A., Berthet, G., Fullekrug, M., Harrison, R. G., Robert, C., Tagger, M., and Gaubicher, B.: In situ detection of electrified aerosols in the upper troposphere and stratosphere, Atmospheric Chemistry and Physics, 13, 11 187–11 194, https://doi.org/10.5194/acp-13-11187-2013, 2013.

Riemer, N. et al.: Aerosol mixing state: measurements, modeling, and impacts, Rev. Geophys., 57, 187–249, https://doi.org/10.1029/2018RG000615, 2019.

Riipinen, I., Sihto, S.-L., Kulmala, M., Arnold, F., Dal Maso, M., Birmili, W., Saarnio, K., Teinilä, K., Kerminen, V.-M., Laaksonen, A., and Lehtinen, K. E. J.: Connections between atmospheric sulphuric acid and new particle formation during QUEST III–IV campaigns in Heidelberg and Hyytiälä, Atmospheric Chemistry and Physics, 7, 1899–1914, https://doi.org/10.5194/acp-7-1899-2007, 2007.

Rycroft, M. J. et al.: An overview of Earth's global electric circuit and atmospheric conductivity, Space Sci. Rev., 137, 83–105, https://doi.org/10.1007/s11214-008-9368-6, 2008.

Stolzenburg, D., Simon, M., Ranjithkumar, A., Kürten, A., Lehtipalo, K., Gordon, H., Ehrhart, S., Finkenzeller, H., Pichelstorfer, L., Nieminen, T., He, X.-C., Brilke, S., Xiao, M., Amorim, A., Baalbaki, R., Baccarini, A., Beck, L., Bräkling, S., Caudillo Murillo, L., Chen, D., Chu, B., Dada, L., Dias, A., Dommen, J., Duplissy, J., El Haddad, I., Fischer, L., Gonzalez Carracedo, L., Heinritzi, M., Kim, C., Koenig, T. K., Kong, W., Lamkaddam, H., Lee, C. P., Leiminger, M., Li, Z., Makhmutov, V., Manninen, H. E., Marie, G., Marten, R., Müller, T., Nie, W., Partoll, E., Petäjä, T., Pfeifer, J., Philippov, M., Rissanen, M. P., Rörup, B., Schobesberger, S., Schuchmann, S., Shen, J., Sipilä, M., Steiner, G., Stozhkov, Y., Tauber, C., Tham, Y. J., Tomé, A., Vazquez-Pufleau, M., Wagner, A. C., Wang, M., Wang, Y., Weber, S. K., Wimmer, D., Wlasits, P. J., Wu, Y., Ye, Q., Zauner-Wieczorek, M., Baltensperger, U., Carslaw, K. S., Curtius, J., Donahue, N. M., Flagan, R. C., Hansel, A., Kulmala, M., Lelieveld, J., Volkamer, R., Kirkby, J., and Winkler, P. M.: Enhanced growth rate of atmospheric particles from sulfuric acid, Atmospheric Chemistry and Physics, 20, 7359–7372, https://doi.org/10.5194/acp-20-7359-2020, 2020.

Svensmark, H. and Friis-Christensen, E.: Variation of cosmic ray flux and global cloud coverage, J. Atmos. Sol.-Terr. Phys., 59, 1225–1232, https://doi.org/10.1016/S1364-6826(97)00001-1, 1997.

Tinsley, B. A.: The global atmospheric electric circuit and its effects on cloud microphysics, Rep. Prog. Phys., 71, 066 801, https://doi.org/10.1088/0034-4885/71/6/066801, 2008.

Tinsley, B. A. et al.: Effects of image charges on the scavenging of aerosol particles by cloud droplets, J. Atmos. Sci., 57, 2118–2134, https://doi.org/10.1175/1520-0469(2000)057<2118:EOICOT>2.0.CO;2, 2000.

Tröstl, J., Chuang, W. K., Gordon, H., Heinritzi, M., Yan, C., Molteni, U., Ahlm, L., Frege, C., Bianchi, F., Wagner, R., Simon, M., Lehtipalo, K., Williamson, C., Craven, J. S., Duplissy, J., Adamov, A., Almeida, J., Bernhammer, A.-K., Breitenlechner, M., Brilke, S., Dias, A., Ehrhart, S., Flagan, R. C., Franchin, A., Fuchs, C., Guida, R., Gysel, M., Hansel, A., Hoyle, C. R., Jokinen, T., Junninen, H., Kangasluoma, J., Keskinen, H., Kim, J., Krapf, M., Kürten, A., Laaksonen, A., Lawler, M., Leiminger, M., Mathot, S., Möhler, O., Nieminen, T., Onnela, A., Petäjä, T., Piel, F. M., Miettinen, P., Rissanen, M. P., Rondo, L., Sarnela, N., Schobesberger, S., Sengupta, K., Sipilä, M., Smith, J. N., Steiner, G., Tomé, A., Virtanen, A., Wagner, A. C., Weingartner, E., Wimmer, D., Winkler, P. M., Ye, P., Carslaw, K. S., Curtius, J., Dommen, J., Kirkby, J., Kulmala, M., Riipinen, I., Worsnop, D. R., Donahue, N. M., and Baltensperger, U.: The role of low-volatility organic compounds in initial particle growth in the atmosphere, Nature, 533, 527–531, https://doi.org/10.1038/nature18271, 2016.

Twomey, S.: The influence of pollution on the shortwave albedo of clouds, J. Atmos. Sci., 34, 1149–1152, https://doi.org/10.1175/1520-0469(1977)034<1149:TIOPOT>2.0.CO;2, 1977.

Yu, F. and Turco, R. P.: From molecular clusters to nanoparticles: role of ambient ionization in tropospheric aerosol formation, J. Geophys. Res., 106, 4797–4814, https://doi.org/10.1029/2000JD900539, 2001.

https://doi.org/10.5194/egusphere-2026-5224
Preprint. Discussion started: 28 September 2026

Zha, Q., Yan, C., Junninen, H., Riva, M., Sarnela, N., Aalto, J., Quéléver, L., Schallhart, S., Dada, L., Heikkinen, L., Peräkylä, O., Zou, J., Rose, C., Wang, Y., Mammarella, I., Katul, G., Vesala, T., Worsnop, D. R., Kulmala, M., Petäjä, T., Bianchi, F., and Ehn, M.: Vertical characterization of highly oxygenated molecules (HOMs) below and above a boreal forest canopy, Atmospheric Chemistry and Physics, 18, 17 437–17 450, https://doi.org/10.5194/acp-18-17437-2018, 2018.

Zhang, L., Gong, S., Padro, J., and Barrie, L.: A size-segregated particle dry deposition scheme for an atmospheric aerosol module, Atmos. Environ., 35, 549–560, https://doi.org/10.1016/S1352-2310(00)00326-5, 2001.